Title
Nanocapsule-based Protein Delivery Platforms for Overcoming Biological Barriers

Author
Wu, Di

Publication Date
2018

Peer reviewed|Thesis/dissertation

UNIVERSITY OF CALIFORNIA

Los Angeles

Nanocapsule-based Protein Delivery Platforms for Overcoming Biological Barriers

A dissertation submitted in partial satisfaction

of the requirements for the degree Doctor of Philosophy

in Chemical Engineering

by

Di Wu

2018

ABSTRACT OF THE DISSERTATION

Nanocapsule-based Protein Delivery Platforms for Overcoming Biological Barriers

by

Di Wu

Doctor of Philosophy in Chemical Engineering

University of California, Los Angeles, 2018

Professor Yunfeng Lu, Chair

As the most dynamic and diverse macromolecules in our body, proteins perform a vast array of function, such as catalyzing metabolic reactions, forming receptors and channels for transportation, responding to stimuli and etc. In this context, tremendous opportunities are provided in harnessing proteins for therapeutic and diagnostic purposes. However, there are still challenges in the development and delivery of protein therapeutics. For instance, the vulnerable nature of proteins with poor stability lead to alternation of protein architects during delivery process which hindered its application. In addition, the low permeability of native protein though biological barriers (e.g., cell membrane, the mononuclear phagocyte system, blood brain barrier, etc.) prevents the successful delivery and efficient response of protein therapeutics. Therefore, development of novel protein delivery platforms, which can stabilize proteins and overcome biological barriers, will broaden the utility of protein therapeutics.

In this dissertation, novel platforms for protein delivery have been developed based on the protein nanocapsule technology, which is achieved by encapsulating the protein molecules with a thin polymer network via in situ polymerization. Such protein delivery platform can significantly improve the protein stability as well as endow various surface properties (e.g., cationic charge, stealth surface, specific targeting capability, etc.) to overcome different biological barriers. Based on this technology, we enable to rationally design and synthesize nanocarriers, understand and precisely control behaviors during transportation process through the biological barriers. This dissertation can be outlined with the following three topics:

1) Fully understand and precisely control the kinetics of intracellular protein delivery. In this part, FLuc nanocapsules, which can mimic current strategies for intracellular delivery, was employed as a probe to real-time quantify the internalization process. By realizing precisely spatiotemporal control over distribution and functions, this platform provides a simple and efficient approach for optimization of dosimetry, characterization of therapeutic efficiency and screening of novel medicine.
2) Overcome the mononuclear phagocyte system to deliver protein therapeutics with prolonged circulation time and reduced immunogenicity. In this work, another FLuc nanocapsule with stealth surface was developed. The probe improves FLuc stability, reduces the immune clearance, prolongs the circulation time and present a high contrast imaging of the tumor. This method provides an effective and safe route for tumor diagnosis.

Overall, this dissertation established various novel strategies toward better protein delivery platforms for overcoming biological barriers, which broaden the application of protein therapeutics.

The dissertation of Di Wu is approved.

Yi Tang

Samanvaya Srivastava

Song Li

Yunfeng Lu, Committee Chair

University of California, Los Angeles

2018

List of Figures

List of Tables

Acknowledgement

On perilous peaks dwells beauty in her infinite variety. I am so grateful that I took the chance to do a doctorate and spent my last six years to learn how to think as a researcher. I would like to thank all the people who supported me during my Ph.D. study.

Foremost, I would like to thank my mentor Professor Yunfeng Lu for his guidance, patience and encouragement throughout my research. He teaches me that life is tough, but life is also good. He opens a new vision of research and teach me how to think something big, learn something new and do something meaningful.

I would like to thank my dissertation committee members, Professor Yi Tang, Professor Samanvaya Srivastava and Professor Song Li for their guidance and help with my research and dissertation.

I would like to express my appreciation of Dr. Yang Liu for his guidance of research as senior members in Lu Lab. And I would like to thank Yilong Yang and Pengcheng Xu, who covers me with the mathematical simulation research. I appreciated Duo Xu for his beautiful and professional scheme pictures. I would like to thank Fang Liu to spend a lot of nice coffee breaks with me. I also would like to thank Dr. Jing Wen, Dr. Meng Qin, Professor Masakazu Kamata and Professor Irvin Chen for the excellent collaboration.

And I would like to take this opportunity to thank all Lu group members and summer students for their helpful discussion and support.

Finally, I would like to express a special thanks to my parents for their encouragement during my study and my husband Jun Ma for his love. They are always the strongest support for me.

Vita

Education

08/2008- **B.S. University of Science and Technology of China**

06/2012 School of Life Science

Research Experiences

09/2012-Present **Ph.D. candidate**

Department of Chemical and Biomolecular Engineering, UCLA

Mentor: Dr. Yunfeng Lu

07/2011-10/2011 **Undergraduate researcher**

Cross-disciplinary Scholars in Science and Technology Program, UCLA

Mentor: Dr. Barney Schlinger

07/2010-07/2012 **Undergraduate researcher**

University of Science and Technology of China

Mentor: Dr. Yunyu Shi

01/2009-07/2010 **Team leader**

"Challenge Cup" National Undergraduate Academic Science Program

Mentor: Dr. Congzhao Zhou

Publications

2018 Real time nanoparticle internalization kinetics assay based on bioluminescence

Di Wu, Yilong Yang, Pengcheng Xu, Duo Xu, Yang Liu, Yunfeng Lu. *Manuscript in preparation.*

2018 Zwitterionic firefly luciferase nanocapsules for cancer diagnosis

Di Wu, Linlin Zhang, Yang Liu, Duo Xu, Yunfeng Lu. *Manuscript in preparation.*

2018 Protein nanocapsules increase central nervous system delivery efficiency via nicotine acetylcholine receptors and choline transporters

Di Wu, Jing Wen, Meng Qin, Duo Xu, George Zhou, Yunfeng Lu. *Manuscript in preparation.*

2016 "An intracellular protein delivery platform based on glutathione-responsive protein nanocapsules." *Chemical Communications* 52, no. 93 (2016): 13608-13611.

Li, Jie, Linlin Zhang, Yang Liu, Jing Wen, **Di Wu**, Duo Xu, Tatiana Segura, Jing Jin, Yunfeng Lu, and Hui Wang.

Presentations

2017 2017 Material Research Society Fall Conference

"Chemiluminescence-Assisted Cell Internalization Kinetics Assay"

Chapter 1. Protein delivery platforms for overcoming biological barriers

1.1 Proteins for therapeutic and diagnostic purposes

As the most dynamic and diverse macromolecules in our body, proteins perform a vast array of function including providing scaffolding support, catalyzing metabolic reactions, transporting molecules from one place to another, forming receptors and channels for transportation, responding to stimuli, DNA replication etc[1–4]. It has been estimated that there are about 1 to 3 billion proteins in the human cell[4]. Any one of these proteins contain mutations, structural abnormalities or irregular level of concentration may result in diseases. Therefore, there is an immense challenge to modern medicines. In this context, tremendous opportunities are provided in harnessing proteins for therapeutic and diagnostic purposes. Since the US Food and Drug Administration (FDA) approved the recombinant insulin in 1982, more than 130 proteins are approved for clinical use.

The first class of protein-based therapeutics with enzymatic or regulatory activities can replace the deficient or abnormal proteins (e.g., insulin[5,6], growth hormone somatotropin[7,8], Protein C concentrate, etc.), augment an existing pathway (e.g., interleukin11, erythropoietin[9,10], filgrastim[11,12], etc.) or provide a novel function. This group of protein therapeutics are applied to replace a particular protein which is deficient or abnormal. For instance, insulin is one of the most widely used protein therapeutics for diabetes. In addition, the proteins for normal protein activity, the protein therapeutics can enhance the magnitude or timing. The erythropoietin, as an example, is a protein hormone secreted by kidney to stimulate erythrocyte production in bone

marrow[13]. Administration of recombinant erythropoietin enables to improve the level of endogenous erythropoietin to normal level in patients with renal failure. Moreover, foreign proteins with novel function can be placed in the body. This type of protein therapeutics can be used for enzymatic degradation of macromolecules such as collagenase (which is used for debridement of cronic dermal uscers and severely burned areas)[14,15], enzymatic degradation of small molecules such as L-asparaginase (which is used for to diminish the exogenous asparagine required by acute lymphocytic leukemia)[16], and haemostasis such as lepirudin (which is used in heparin-induced thrombocytopaenia)[17].

Targeted proteins, include monoclonal antibodies and immunoadhesins, exquisitely bind to recognition site or receptors to guide immune attack on targeted molecules or cells. This kind of protein therapeutics are widely applied in cancer therapy (e.g., bevacizumab[18,19], rituximab[20–22], trastuzumab[23], etc.), immunoregulation (e.g., abatacept[24], anakinra[25], adalimumab, etc.) and transplantation (e.g., antithymocyte globulin[26], basiliximab[27], dacilizumab[28], etc.). One of the great challenges for drug therapy and delivery is the bioselectivity to specific targeting site, which is essential in both improving therapeutic efficacy and reducing side effects. Such targeted protein enables special targeting activity to influence the metabolism, stimulate or block a signaling pathway and induce destruction. In addition, it also can be combined with other therapeutic molecules to improve their selectivity.

To develop effective immunity against infectious disease or cancer cells, the immune system must be activated first. Proteins can also be produced as protein vaccines to protect against a deleterious foreign agent, treat an autoimmune disease or treat cancers. By administration of immunogenic but non-pathogenic protein vaccines, immunity can be activated

without exposed to the risk of infection. Examples include the recombinant hepatitis B vaccines[29,30], which is created by producing the hepatitis B surface antigens. Besides protecting against foreign invaders, proteins can be provided arise immunological acceptance. For example, a pregnant woman may reject a fetus if she has been immunized against certain antigens before. Administration of the antibodies prevents the woman to develop antibodies against fetus antigens, avoiding the pregnancy loss[31].

Besides employed as therapeutics, proteins can also serve as diagnostics. The application of such kind of proteins includes in vivo infectious disease diagnosis, cancer diagnosis and in vitro diagnosis. Imaging agents such as enhanced fluorescent protein (EGFP) and firefly luciferase (FLuc) can be adopt as an indicator in metabolism process. In addition, the protein hormones can be used to diagnose endocrine disorders. For example, the growth hormone releasing hormone (GHRH) can be used to as biomarkers of pituitary growth hormone secretion in the patients with growth hormone deficiency[32].

Compared with the small-molecule drugs, proteins therapeutics are high specific, which provides enhanced therapeutic efficiency as well as reduced side effects. In addition, the effective replacement treatment by protein delivery without gene alternation is faster and safer. Currently, due to the development of recombinant gene technology, recombinant proteins can be produced from a wide range of organisms, such as bacteria, yeast, mammalian cells, transgenic animals and plants[33–36].

Though many successful protein therapeutics and diagnostics have been made, there still are a number of challenges in development and delivery of protein therapeutics. One of the

challenges is the stability of proteins[37]. As a macromolecule, the retention time of proteins are drastically affect by temperature, protease and immune clearance after administrated[38]. In addition, to be delivered into targeting site, the proteins need to overcome many biological barriers, such as the cell membrane and the blood brain barrier. Protein engineering can improve the some of the in vivo behavior. However, it takes a lot of time and labor. In addition, comparing with the requirements, limited protein therapeutics have been well engineered. Therefore, novel platforms, which can easily improve protein stability, evade immune clearance and increase delivery efficiency across biological barriers, need to be developed. In addition, methods for precise characterization of the protein therapeutics need to be investigated for safety concerns. The structure of each biological barriers and recent approaches to delivery protein therapeutics across such biological barriers will be discussed in the following sections.

1.2 Biological barriers

After administrated into patients, various biological barriers prevent the successful delivery and efficient response of protein therapeutics. For instance, the drugs undergo opsonization and clearance by the mononuclear phagocyte system (MPS), which limited the bioavailability to targeting site. In addition, a lot of protein therapeutics need to be delivered into the cells to exert their functions. The cellular internalization and endosomal escape are formidable barriers as well. To achieve central nervous system (CNS) delivery of protein therapeutics, the proteins need to penetrate through the blood brain barrier (BBB) which is a highly selective barrier separates the circulating blood from the CNS.

Due to the biological barriers, the inability to reach therapeutic levels of protein

therapeutics at target site is regarded as the major limitation of protein delivery. Successful delivery of proteins requires rational design of carriers to address all these biological barriers. The details of each biological barrier, including cell membrane, MPS and BBB are described as below.

1.2.1 Cell membrane internalization

The cell membrane is a biological membrane, which separated the interior of cells from the extracellular environment[39]. It consists of a lipid bilayer with embedded proteins. As a selectively permeable membrane, it restricts and regulates the substance transport in and out of cells. To achieve its function, several transport mechanisms are involved by the cell membrane.

The small and nonpolar molecules including oxygen and carbon dioxide penetrate the cell membrane by simple diffusion, driven by the concentration gradient between inside and outside of the cells. This is a passive transport process without incorporation of energy or receptors. Some of the nutrients (e.g., amino acids, glucose, choline, etc.) and ions transport through the plasma membrane via transmembrane protein channels or transporters. Energy or transporters are involved during the transportation process. In addition, most of the macromolecules such as proteins and genes need to be internalized through endocytosis pathway, that the macromolecules were engulfed by enclosing them in membrane vesicles.

Generally, endocytosis process can be divided into two different categories, phagocytosis and pinocytosis. The phagocytosis pathway occurs in the specialized cells, such as macrophages, monocytes and neutrophils, which can engulf and clear pathogens (e.g., bacteria, yeast) or the

large debris[40]. To active this process, specific receptors including the complement receptors and phosphatidylserine receptors, on the cell surface are required to induce the signaling cascades of Rho-family GTPases[41,42].

Instead of restricted to specialized mammalian cells like phagocytosis, the pinocytosis pathway is found in all of the cells, which can be divided to four mechanisms including macropinocytosis, clathrin-mediated endocytosis, caveolin-mediated endocytosis and clathrin and caveolin-independent endocytosis. The macropinocytosis is induced upon the simulation of signals such as growth factors. Similar to phagocytosis, the Rho-family GTPases are involved to mediate the signaling cascades in micropinocytosis pathway[43]. But instead of 'zipper up' along the particle, macropinocytosis collapse onto and fuse with the cell membrane during the endocytosis. The caveolae-mediated endocytosis is slow (the half-time of which is more than 20 min) and the volume of vesicles are small (about 50-60 nm in diameter)[44,45]. The clathrin-mediated endocytosis occurs constitutively in all mammalian cells to uptake the nutrients. Involved by the receptors on the cell surface, the clathrin-mediated endocytosis is also crucial for intracellular communications, cell and serum homeostasis and recycling of synaptic vesicle membrane proteins after neurotransmission[46]. In addition, the clathrin- and caveolin-independent endocytosis occurs when some bacteria and virus to access to the host cells, in which the clathrin or caveolin are not incorporated[47].

To fulfil the therapeutic and diagnostic purposes, the proteins need to be delivered inside cells to reach their biological targets. However, across the cell membrane is challenging due to semi-permeable the nature of such lipid bilayer.

1.2.2 Mononuclear phagocyte system sequestration

The MPS is consisted by phagocytic cells and macrophages in the spleen, liver and lymph nodes, which sequesters the drugs immediately after systematic administration. The sequestration process is firstly achieved by opsonization of drugs via the adsorption of plasma proteins such as complement components, immunoglobulins, serum albumins and apolipoproteins[48,49]. Such opsonins are distributed throughout the blood. After injection of the protein therapeutics, they contact with the drugs by Brownian motion, flowed by attractive forces including Van der Waals, electrostatic ionic and hydrophobic interactions to bind onto the surface of the drugs.

Attachment of the drugs to the surface of phagocytes is then induced by opsonization as the second step of clearance process. There are three methods for the phagocyte attachment[50,51]. The first methods incorporate the specialized receptors on the surface of phagocytes that can recognize the foreign material with the bound opsonin proteins and undergo conformational changes. Besides specific binding to the receptors, non-specific adherence of the adsorbed serum proteins to the phagocytes surface via the hydrophobic interaction can induce the attachment as well. In addition, the complement activation, include the classical, alternative and lectin pathway, is another method to initiate the phagocyte attachment.

The phagocytes will engulf the attached foreign materials by endocytosis. The internalized materials were then exposed to enzymes and oxidative-reactive chemicals (e.g., hydrogen peroxide, superoxides and nitric oxide, etc.) and finally breakdown.

Therefore, due to the sequestration of the MPS, the final biodistribution of protein therapeutics generally end in the MPS organs instead of targeting site. The novel approaches to evade the MPS clearance and prolong the circulation time of protein therapeutics is the basement for successful targeting delivery.

1.3 Nanocarriers for protein delivery

Currently the nanotechnology has been well developed for the delivery of protein therapeutics. Nanocarriers, which have a size in the scale of nanometers, are engineered and applied to medical research and applications. In such size range, the carriers exhibit unique properties such as optical, electrical and magnetic characters. A wide range of materials including in-organic materials (e.g., metals, metal oxides, semiconductors, etc.) and organic materials (e.g., lipids, polymers, etc.) can be involved as potential candidates[64].

Liposomes, for instance, forms by a lipid bilayer encapsulating an aqueous phase in side to carry drugs. Using different kind of lipids, the liposome can be modulated with different surface properties, such as cationic surface, neutral surface or pH-responsive surface. Polymeric nanoparticles are another fully investigated drug carriers[65]. Proteins can be adsorbed or covalent linked to the polymers and delivered to the target site. Nanoparticles can also be synthesized using inorganic materials, such as gold nanoparticles, mesoporous silica, carbon nanotubes and etc.

Due to the physical and chemical properties of nanoparticle-based protein delivery platforms, it is regarded as a potential candidate for overcoming the biological barriers to achieve

efficient delivery to the targeting site. The current strategies of nanoparticles for to address the biological barrier including the plasma membrane, MPS and BBB are described in the following sections.

1.3.1 Nanocarriers for intracellular delivery

In order to intracellular deliver protein therapeutics, the nanoparticles have to transverse the cell membrane. The synthetic nanoparticles can be engineered with various properties to facilitate the transport through the cell membrane[66].

Since the cell membrane is negatively charged, cationic coating on the surface of nanoparticles, which can interact by the electrostatic force with the cell membrane, is one of the most commonly adopt methods. It can be achieved using the cationic liposomes (e.g., lipofectamine), polypeptides (e.g., polylysine) and amine-containing polymers (e.g., polyethleneimine)[67]. The cationic nanoparticle enables improved cell membrane permeability. However, the cytotoxicity and poor stability restrict its application[68,69].

The cell penetrating peptides (CPPs), which are peptides with specific sequence less than 30 amino acids, are another approach to address the cell membrane barrier by conjugating onto the surface of nanocarriers[69]. Currently, a number of CPP sequence have been discovered from the natural sequences such as TAT (from HIV protein)[70,71], penetratin (from homeodomain)[72], transportan (from galamin-mastroparan)[73] and etc.

In addition, conjugating targeting ligands to the nanoparticles, which can bind with antigens or receptors on the surface of cell membrane, can enhance the selectivity of cell

internalization to specific cell types. The strength of interactions between nanoparticles and cell surface can be adjusted by varying the type and the density of targeting ligands. A large variety of candidates can be selected as targeting moieties, such as antibodies, peptides, aptamers, vitamins and etc[74–76].

1.3.2 Nanocarriers for systematic delivery

In order to achieve successfully systematic delivery of protein therapeutics, the nanoparticles need to address MPS barrier, allowing a long circulation time in the plasma[77]. Since the opsonization of nanoparticles initiate the following phagocytic recognition and clearance, the current strategies to evade MPS clearance is endowing neutral charged and stealth surface properties on the nanoparticles to block the opsonization. The most commonly used material is the polyethylene glycol (PEG). The stealth surface properties of PEGylated nanoparticles increase the capability to resist protein adsorption and evade clearance of immune cells. Consequently, the pharmacokinetics and biodistribution profiles will be improved by PEGylation[78].

1.4 Protein nanocapsules

Recently, our group has developed a platform technology named as protein nanocapsules to deliver proteins for various therapeutic applications[85]. As illustrated in Figure 1-1, this is achieved by an encapsulating technique, in which each protein molecule is encapsulated by a thin shell of polymer by *in situ* polymerization.

The synthesis process of the protein nanocapsules involves two steps. The protein cores are first conjugated or adsorbed with polymerizable vinyl groups on the surface. Mixing the proteins with monomers and crosslinkers, the monomers and crosslinkers are condensed around the protein via noncovalent interactions. Then in situ polymerization can be initiated to achieve a thin layer of polymer wrapping the protein molecules.

This protein delivery platform endows the protein therapeutics with several advantages. For instance, the polymer shells improve the stability of protein molecules especially against proteolysis and non-physiological environment. The size of the nanocapsules are generally around 20 to 30 nm, which is favorable for systemic circulation. The polymer shell allows transportation of small molecules such as substrates. Consequently, the native activity of proteins is maintained after encapsulation.

Incorporated with the degradable crosslinkers, the protein cargos can be released in a controllable manner. For instance, protein nanocapsules can be constructed using crosslinkers responded to the changes in the local physiological environment (*e.g.*, pH, tumor-specific proteases, and matrix metalloproteases), allowing degradation of the polymer shell and the release of the protein under certain conditions[86–88]. This design particularly provides a novel approach to delivering growth factors (*e.g.*, bone morphogenetic protein 2 (BMP-2), vascular endothelial growth factor (VEGF), platelet–derived growth factor (PDGF), and nerve growth factor (NGF)) for bone healing, angiogenesis, and neuroregeneration[89].

In addition, by varying the monomers and crosslinkers, the surface properties of the protein nanocapsules is highly turntable. A family of protein nanocapsules with controlled

surface chemistry and physiological behavior have been synthesized for overcoming the biological barriers upon different therapeutic demands. For example, protein nanocapsules with different cationic surface charges is synthesized for intracellular delivery of protein therapeutics. The surface can be further modulated with PEG, CPPs and targeting moieties[85].

Zwitterionic protein nanocapsules with prolonged circulation time and reduced immunogenicity have been made for the therapeutic purposes for gout and other metabolic disorders and diagnostic purposes for cancer imaging through systemic administration[90].

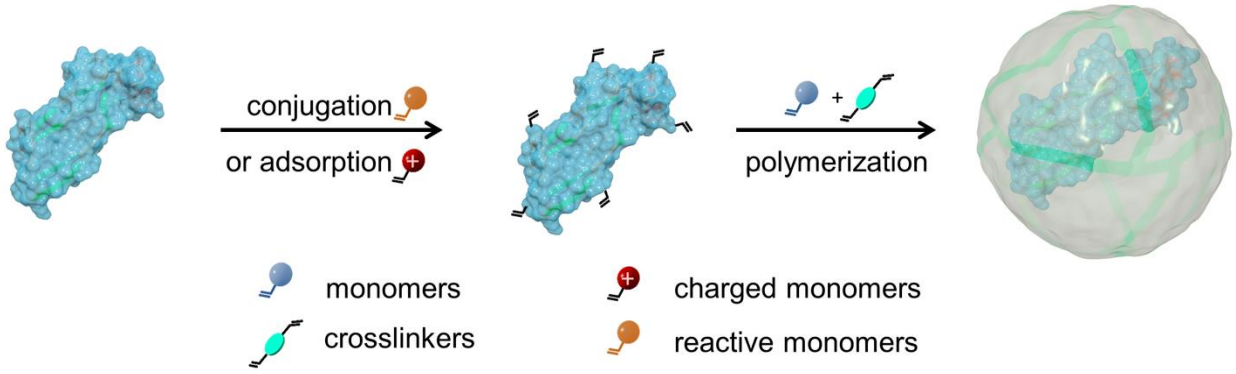

Figure 1-1. Schematic illustration of the design and synthesis of protein nanocapsules via i*n situ* polymerization to form a thin layer of polymer shell along the protein molecule. The protein nanocapsule is synthesized by firstly conjugate or adsorbed with polymerizable vinyl groups on the surface, followed by in situ polymerization to form the polymer shell.

1.5 Dissertation objectives and research scope

The objective of my dissertation is to develop, characterize and control protein delivery

platforms to overcome the biological barriers via the protein nanocapsule technology. Briefly, my dissertation is dedicated to the following aspects:

(1) Develop protein nanocapsules for intracellular protein delivery that enables quantitative and real-time monitoring kinetics of internalization based on FLuc nanocapsules. (Chapter 2)

(2) Develop protein nanocapsules for systematic protein delivery and apply it as a novel bioluminescent probe of extracellular ATP based on FLuc for tumor diagnosis with high sensitivity and high specificity. (Chapter 3)

Chapter 2. Real Time Nanoparticle Internalization Kinetics Assays Based on Bioluminescence Nanocapsules

2.1 Introduction

A cell is the basic functional and biological unit of living organisms. Cell membranes serve as a physical barrier separating the intracellular content from the extracellular space; substances are selectively translocated crossing the membranes to maintain the cellular function[91]. Beyond this natural biological process, there have been great interests to deliver biomolecular molecules such as proteins and genes into cells for gene editing, cell reprograming, therapy, and other purposes[92–95]. Such intracellular delivery is generally based on nanoparticular vectors; quantifying the internalization kinetics is of particular importance, which may provide essential parameters (e.g., rate of internalization, delivery efficiency, cell selectivity and targeting ability) towards better delivery outcomes[96,97].

To achieve effective intracellular delivery, cationic lipids and polymers are commonly used, which are assembled with cargo molecules forming nanoparticles with positive charge[98,99]. Different functional moieties, such as cell penetrating peptides[100–102], targeting components[103,104], and poly(ethylene glycol) (PEG) are often conjugated to the nanoparticles, which enhance the cell penetrative capability, provide targeting capability, reduce cytotoxicity, and prolong the circulation time of the nanoparticles[105]. To examine the internalization process, fluorescent microscopy and fluorescence-activated cell sorting (FACS) techniques are the most used tools[106–109]. Both the methods, however, require pre-treatment steps (e.g., rinse, fixation or detachment), which could only capture snapshots of an internalization process at specific time points. Without extra treatment, it is often difficult to distinguish the fluorescent signals from

the fluorophores within the cells or bounding on the cell membranes. Moreover, intensity assessment of internalized nanoparticles via fluorescence-based methods is in which is dependent on individual measurement apparatus. In this context, it is incapable to compare results among different research. Inorganic nanoparticles (e.g., gold and iron oxide) are also employed as model vectors, the amounts of which internalized by cells at specific time points are quantified by atomic absorption spectroscopy, electron microscopy or magnetophoresis[110,111]. Similar to the fluorescent-based strategies, these methods can only provide the information of the internalization process in discrete time.

In this chapter, we report a real-time nanoparticle internalization kinetics assay (RNIKA) based on bioluminescent nanoparticles. Bioluminescence commonly exists in living organisms; one example is firefly luciferase (FLuc), which catalyzes the oxidation of luciferin in presence of adenosine-5'-triphosphate (ATP), accompanied by light emission[112,113]. ATP is the most common phosphate donor in cells, the concentration of which in the cytosol (1-10 mM) is substantially higher than that in extracellular environment (1-1000 nM)[114,115]. The significant difference of the ATP concentration crossing the cell membranes enables the use of FLuc as effective probes for cell internalization. The abrupt increase of the ATP concentration during cell internalization process promotes the bioluminescent reaction within the cells, leading to high sensitivity with low background. Consequently, a library of FLuc nanoparticles with tunable surface charge, cell penetrative moieties, targeting moieties, and PEG moieties were synthesized and delivered to various cell lines, during which bioluminescence is recorded and converted to real-time internalization kinetics of the nanoparticles. Since FLuc nanoparticles can be made with the essential characteristics resembling most nanoparticulate vectors of interest, this method

provides a class of bioluminescent nanoparticular analogues enabling fast quantification of real-time cell internalization kinetics of nanoparticles.

2.2 Results and Discussion

To synthesize such a library of FLuc nanoparticles, an *in situ* polymerization technique was used. Briefly, FLuc molecules are first conjugated with polymerizable acryl groups and added to an aqueous solution containing acrylamide (AAM, neutrally charged monomer), N-(3-aminopropyl) methacrylamide (APM, positively charged monomer) and N,N'-methylenebisacrylamide (BIS, crosslinker). Driven by noncovalent interactions, the monomers and crosslinker are enriched around individual FLuc molecules and polymerized to construct a thin polymer shell encapsulating the FLuc molecules, forming FLuc nanocapsules denoted as nFLuc. Tuning the amount of APM used enables the synthesis of nFLuc with tunable surface charge and various functional moieties could be readily conjugated to the nanocapsules, affording the construction of a library of bioluminescent nanoparticles with tailored characteristics.

Successful construction of nFLuc with tunable surface charge was demonstrated in Figure 2-1Ai. Six nFLuc with surface charges proportionally increased from 0 mV to 15mV were synthesized by tuning the ratios of APM to AAM from 0:5600 to 1000:4600 while maintaining the ratio of the total monomers to FLuc as 5600:1. These nanocapsules, on the other hand, exhibit a similar diameter in the range of 21 nm to 28 nm. Using nFLuc(6mV) made with a APM/AMM ratio of 400:5200 as a representative, the transmission electron microscope (TEM) image exhibits spherical morphology with a uniform diameter around 25 nm (Figure 2-1Aii).

Figure 2-1Aiii and 2-1Aiv further compare size distribution and zeta potential of native FLuc and APM200 obtained by dynamic light scattering (DLS). APM200 shows a narrow size distribution centered at 25 nm and a positive surface charge of 6.8 mV in comparison that of the native FLuc at 8 nm and -7.9 mV, respectively, indicating successful encapsulation of the FLuc with a cationic polymer shell. Our previous work has demonstrated that such nanocapsules generally contain a single molecule of protein. The thickness of the polymer shell estimated around 9 nm based on the DLS result. The thin polymer shells improve the stability of the FLuc while allows effective transport of luciferin and ATP.

Such bioluminescent nanocapsules can be conjugated with various functionalities to imitate those of nanoparticles commonly used for intracellular delivery. For example, nFLuc(9mV) made with APM/AMM 600/5000 were conjugated with PEG2000 (molecular weight 2000) at a molar ratio of 12:1 and 23:1, forming PEGylated nanocapsules denoted as PEG1-nFLuc and PEG2-nFLuc, respectively. Cell internalization of the nanocapsules in 4T1 cells was investigated by fluorescence microscope (Figure 2-1Bi) and FACS (Figure 2-1Bii). The cells incubated with the PEGylated nFLuc exhibit significant reduction in fluorescent intensity indicating reduced phagocytosis. Compared with nFLuc(9mV), FACS illustrates that the cell internalization of PEG1-nFLuc and PEG2-nFLuc is decreased to 71% and 46%, respectively. nFLuc(9mV) was conjugated with RGD peptides (denoted as RGD-nFLuc) and delivered to three different cell lines 4T1, A549 and Hela. As expected, A549 and Hela cells with overexpressed RGD receptors, integrin $\alpha_v\beta_3$, show more effective uptake than 4T1 cells after one-hour incubation (Figure 2-1Ci) with 1.5-fold and 1.2-fold increase in cell uptake, respectively (Figure 2-1Cii). TAT, the first cell penetrative peptide (CPP) discovered from HIV-1 virus, was also conjugated to APM600 (denoted as TAT-nFLuc). As expected, 4T1 cells

incubated with TAT-nFLuc show significantly higher fluorescent intensity (Figure 2-1Di); FACS suggests a 2.6-fold increase of uptake in comparison with APM400 (Figure 2-1Dii).

These examples suggest that various functional moieties could be readily conjugated to nFLuc just like to nanoparticles that are commonly used for intracellular delivery. Such capability enables the synthesis of a nFLuc library with the essential characteristics resemble those of the existing nanoparticlular vectors. Note that size of the nanoparticles does significantly affect the internalization process. Based on the energy required to deform a cell membrane upon an internalization process, it has been shown that nanoparticles with diameter in the range of 20-30 nm require the least energy consumption. Such bioluminescent nFLuc with the optimized size for cell internalization, tunable surface charge, targeting capability, and enhanced cell penetrative capability offers real-time probes for cell internalization kinetics of

nanoparticles.

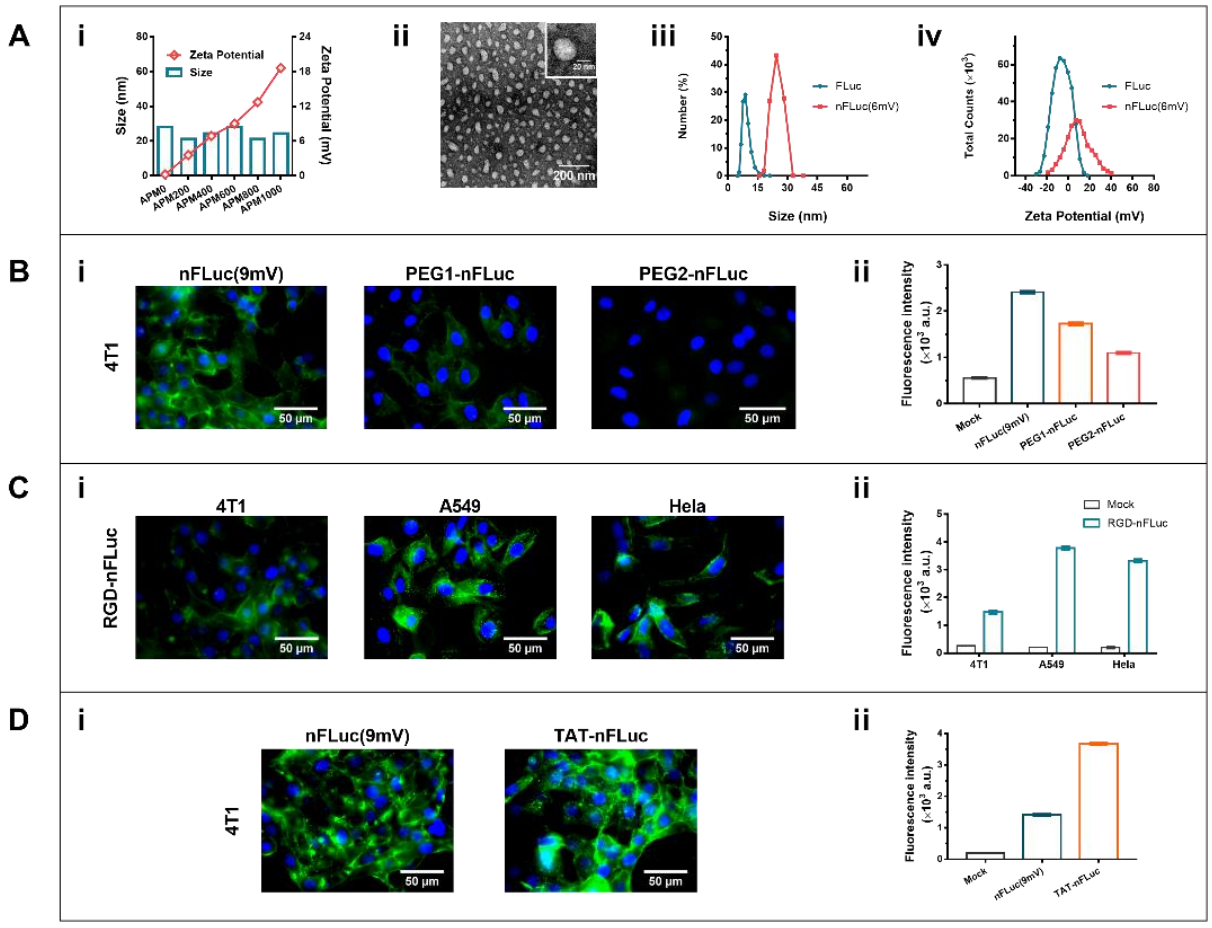

Figure 2-1. Firefly luciferase nanocapsules (nFLuc) which resemble the physicochemical properties of various nanoparticles for intracellular delivery. (A) Synthesis of nFLuc with different surface charges. **(Ai)** The steady size and tunable surface charge of nFLuc with six relative ratios of positively charged monomer (APM). **(Aii)** TEM images of nFLuc(6mV) indicating a uniformed sphere of 25 nm in diameter. **(Aiii)** The size distribution of FLuc and nFLuc(6mV). **(Aiv)** The zeta potential distribution of FLuc and nFLuc(6mV). **(B)** PEGylation of nFLuc. **(Bi)** Fluorescent images illustrating the internalization efficiency of nFLuc and PEGylated nFLuc with two ratios of PEG2000 in 4T1 cells. **(Bii)** Histogram comparing the mean

fluorescence intensity from FACS analysis of nFLuc and PEGylated nFLuc with two ratios of PEG2000. Mean ± SEM, n=3 **(C)** The conjugation of the targeting agent RGD on nFLuc. **(Ci)** Fluorescent images illustrating the internalization efficiency of RGD-nFLuc in 4T1, A549 and Hela cells. **(Cii)** Histogram comparing the mean fluorescence intensity from FACS analysis of the internalization efficiency of RGD-nFLuc in 4T1, A549 and Hela cells. Mean ± SEM, n=3 **(D)** The conjugation of TAT on nFLuc. **(Di)** Fluorescent images illustrating the internalization efficiency of nFLuc and TAT-nFLuc in 4T1 cells. **(Dii)** Histogram comparing the mean fluorescence intensity from FACS analysis of nFLuc and TAT-nFLuc in 4T1 cells. Mean ± SEM, n=3.

Figure 2-2C illustrates the internalization of nFLuc by a cell pre-incubated with luciferin, during which the internalized nFLuc catalyzes the reaction of luciferin and ATP and emits bioluminescence. To confirm that bioluminescence could only be produced after the nFLuc is internalized into the cytosol, 4T1 cells were incubated with fluorescein-labelled nFLuc(6mV) (made with APM/AAM 400/5200) and nFLuc(0mV) (made with APM/AMM 0/5600). The cells incubated with nFLuc(6mV) show significantly higher fluorescent intensity than those with nFLuc(0mV) (Figure 2-2A), suggesting more effective internalization of nFLuc(6mV) due to its positive charge. Consistently, nFLuc(6mV) and nFLuc(0mV) show minimal light emission (< 50 RLU) in the absence of cells or ATP (Figure 2-2B). 4T1 cells incubated with nFLuc(6mV) and nFLuc(0mV) show bioluminescence intensity of 6174 RLUs and 52 RLUs, respectively. Adding 10 mM ATP into the cell culture medium increases the luminescence intensity to 7050 and 2599 RLUs, respectively. Therefore, the internalization of nFLuc into the cell cytosols, only where sufficient ATP presents, is the determining step for bioluminescence emission.

The cell internalization kinetics of nFLuc can be achieved by monitoring the real-time bioluminescence emission by

$$RLU_t = \frac{K_{cat}[S]}{K_M + [S]}[nFLuc]e^{-k_d t} \cdot A \cdot N$$

where RLU_t is the relative light units produced via bioluminescence reaction per second (*RLU*/s), *N* is the number of cells in a well of 96-well plates, and *A* is a conversion factor between *RLU* per mole of luciferin reacted, which is 5.73 x10^9 *RLU*/mol[113]. The term $\frac{K_{cat}[S]}{K_M+[S]}[nFLuc]e^{-k_d t}$ represents the rate of reaction of luciferin, where K_{cat} and K_m are the turnover number and Michaelis constant of nFLuc measurable using the Lineweaver-Burk plot, and [S] and [nFluc] are the concentration of luciferin and nFLuc in the cytosol, respectively. Since the amount of luciferin in the cytosol consumed during the kinetics measurement is negligible compared with the initial luciferin concentration in the cytosol [S_0] (2.0 mM), [S] is taken as a constant of 2.0 mM. The term $e^{-k_d t}$ is applied herein to compensate the activity decay of nFLuc with time (*t*), where k_d is the activity decay constant measured from the *RLU*-time profiles using the Hough Transform method. Detail information is provided in the experimental section.

Figure 2-2D shows a representative profile of RLU_t collected from 10^5 4T1 cells incubated with 0.4 mg/mL of nFLuc(6mV) (Figure 2-2D). The decay constant k_d of nFLuc within 4T1 cells is estimated as 1.08×10^{-3} s^{-1}, which is close to the k_d in cell lysate (3.34×10^{-4} s^{-1}). The K_m and K_{cat} were measured as 0.31 mM and 0.022 s^{-1} in turn. Accordingly,

intracellular concentration of nFLuc(6mV) (nM) can be calculated and illustrated in Figure 2-3E. The cellular uptake of nFLuc grows linearly at the initial stage, and reaches a plateau of 0.49 nM at 33 min. The half maximal internalization time was 12.6 min. To confirm the reliability of this approach, 4T1 cells incubated with 0.4 mg/mL nFLuc(6mV) were fixed at different timepoints, and the mean fluorescence intensity was analyzed via FACS (Green open cubes, Figure 2-2E). Figure 2-2F further shows the internalization kinetics of nanocapsules made from FITC-labeled bovine serum albumin (BSA) (denoted as nBSA) obtained by FACS. These nBSA, synthesized with the same formulation as nFLuc(6mV), show a well-fitted kinetic profile with that of nFLuc(6mV). This comparison further suggests the internalization kinetics are majorly determined by their surface characteristics rather by the protein encapsulate.

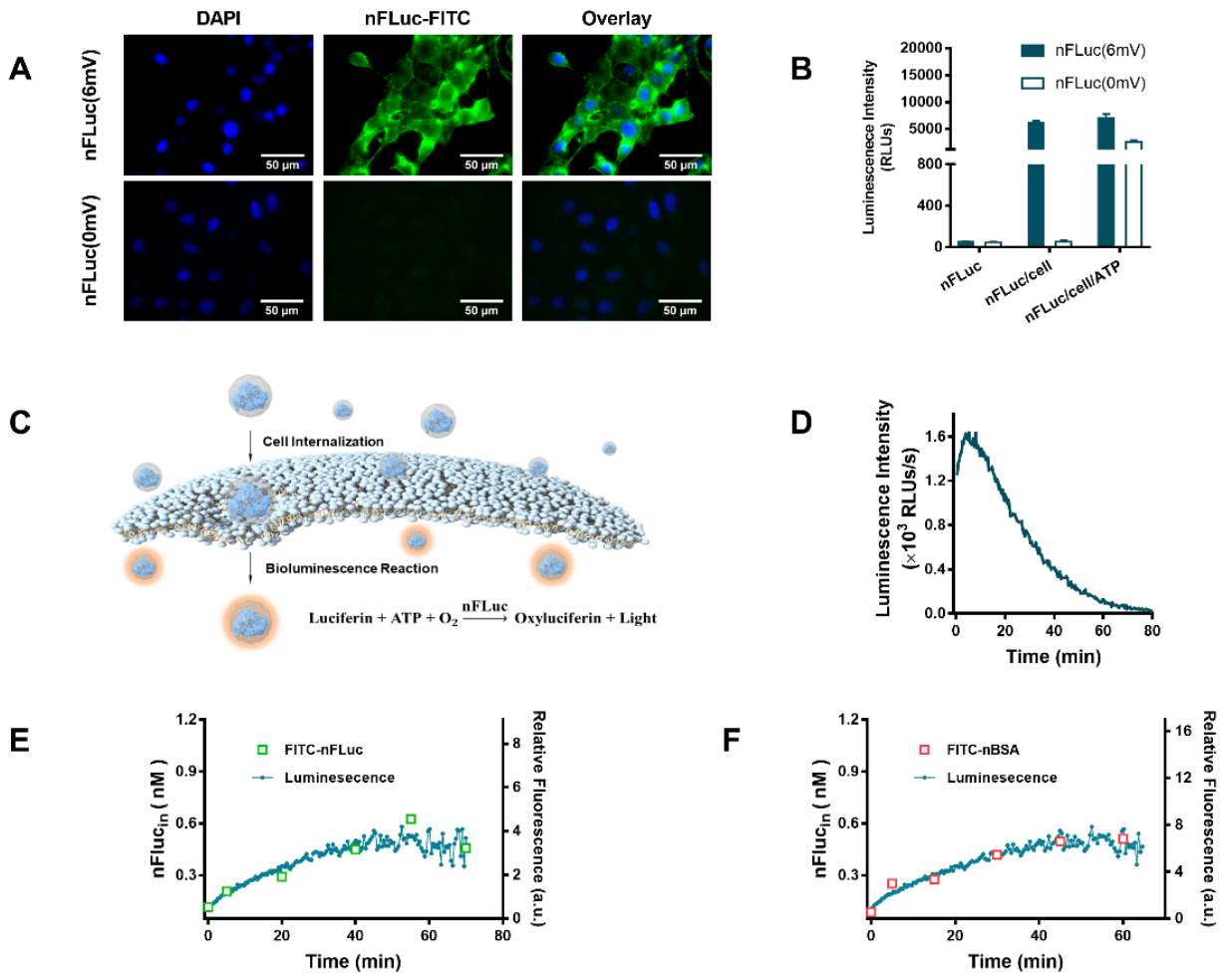

Figure 2-2. Cell internalization kinetics measurement. (A) Fluorescent images illustrating the internalization efficiency of nFLuc (6mV) and nFLuc (0mV). **(B)** Bioluminescence intensity comparison of nFLuc (6mV) and nFLuc (0mV) with and without cells and ATP addition. **(C)** Schematic illustration of luciferase nanocapsules (nFLuc) internalization, bioluminescent reaction and math model for internalization kinetics simulation. Cell internalization: nFLuc are internalized via endocytosis after adsorbing on the cell membrane. Bioluminescence reaction: luciferin is catalyzed by nFLuc with ATP in cytosol, resulting in light emission. Internalization kinetics can be directly monitored and quantified by detecting bioluminescent intensity. **(D)**

Time course of bioluminescence intensity profile of 4T1 cells incubated with nFLuc (6mV). **(E)** The kinetics profile of nFLuc (6mV) internalization, compared with FACS results of FITC-labelled nFLuc (6mV). **(F)** Comparison between nFLuc (6mV) kinetics profile and internalization of FITC-labelled nBSA synthesized with the same formulation measured by FACS.

The RINIA provide a unique tool to quantify kinetic parameters of nanoparticles with different chemical properties, such as surface charge and conjugation of targeting ligands. Since the difference of ATP concentration between cytosol and extracellular space, RINIA is capable to monitor the internalization process without pre-treatment steps, allowing a real-time monitoring of the cell internalization. Instead of using an arbitrary unit, the quantification of internalized nanoparticles can be achieved through a simple modified Michaelis Menten equation. Moreover, the parameters incorporated in the kinetics quantification such as k_d, K_M and K_{cat} are all achieved from experiments, which diminish individual difference among cell lines and nanoparticles.

Previous investigations signpost that nanoparticles with more positive surface charge implied improved delivery efficiency and higher rate of internalization, but also higher cell toxicity. However, quantitative description of cell internalization kinetics including the efficacy, the rate, and the time profile with nanocapsules with different surface charges remains unclear. To pinpoint effects of surface charge on the internalization kinetics, three types of nanocapsules were prepared with surface charge as 3 mV, 6 mV and 9 mV, and named as ‘Charge 1+’, ‘Charge 2+’, and ‘Charge 3+’, respectively (Figure 2-3Ai). All three nanocapsules had similar particle size as ~28 nm, which minimized the size preference during internalization. Figure 2-

3Aii summarizes the internalization kinetic profiles of 4T1 cells incubated with 6.56 μM of the nanocapsules. As expected, the plateau concentrations of the three nanocapsules are increased with the increasing surface charge, quantified as 0.44, 1.09 and 2.74 nM, respectively.

To further illustrate the impact of surface charge under different dosages, the initial rates (Figure 2-3Aiii), the half-lives (Figure 2-3Aiv), the plateau concentrations (Figure 2-3Av) and efficacy (Figure 2-3Avi) were investigated within the range of initial doses from 0.66 μM to 6.56 μM. As illustrated in Figure 3Aiii, the internalization rates satisfy a linear growth over [$nFLuc_{out}$] when charge is below 6 mV or initial concentration level is lower than 4 μM. It indicates that the cell internalization of three nanocapsules with increasing surface charge followed 1^{st} order reaction with a rate constant of 2.74 s^{-1}, 4.51 s^{-1}, and 11.61 s^{-1} in turn, when the rates were in linear range. As the concentration of the nanocapsule with 9 mV-surface charge is higher than 4 μM, the rate of internalization exhibits a burgeon that deviated from the original linear progression. The plateau concentration of internalization behaves in the similar pattern (Figure 2-3Av), while the half-lives (Figure 2-3Aiv) and the efficacy (Figure 2-3Avi) of all three nanocapsules turn to be in linear regression.

This result is distinct from thermodynamic equilibrium, which shows a uniform partition coefficient (the concentration of nanoparticles inside of cells over the concentration outside the cells at the steady state) with different dosages. However, the partition coefficient based on bioluminescence assay increases monotonically when the initial concentration of nanocapsules is increased (Figure 2-3Avi). These results reveal that the internalization of cells is a more complicated process besides attaining the thermodynamic equilibrium of cell membrane. The

change of membrane permeability and the bioenergy involved in function maintenance as a living organism are worthy of consideration.

Cell internalization kinetics is cell-state-dependent, suggesting different internalization kinetic profiles occur upon cell stimulation. This nFLuc assay enables a detailed understanding of the cell internalization process during different state of cells. For instance, peripheral blood mononuclear cells (PBMC), which are the major immune cells in blood, show varying cell behaviors upon stimulation. Only when we understand the internalization kinetics of nFLuc in PBMC in both quiescent and stimulated status, will we predicate and design regimens within minimum effect but maximum tolerant dosages for different purposes. As showed in Figure 2-3Bi, the internalization kinetics of nFLuc (6mV) in PBMC with and without simulation are compared in intracellular concentration of nFLuc by detecting the produced bioluminescence in real-time. With stimulation, the plateau concentration of nFLuc increased 2.2 times from 7.16 nM to 15.93 nM.

Different cell types also present diverse behaviors of cell internalization process, so quantification of the kinetics profiles allows optimal material design for specific cell types. Figure 2-3Bii illustrates the different internalization kinetics between macrophage cells J774A.1 and the brain endothelial cell bEnd3. The macrophage J774A.1 cells, which are active to engulf foreign substances for immune clearance, uptook 6.09 nM of nFLuc (6mV) to reach the plateau concentration. Meanwhile, the brain endothelial cell bEnd3, which pose an obstacle to drug delivery to the brain, present a 10-fold lower level of plateau concentration (0.66 nM) than that of J774A.1. This comparison indicates that nanocapsules for brain delivery needs optimization

based this positively charged formulation, because with current condition, most nanocapsules will be internalized by macrophage cells other than brain endothelial cells.

Different surface modification of nanoparticles endows them various capability. PEGylation, for example, possesses a number of physicochemical and biological properties, including solubility, biocompatibility and stealth capability form systemic barrier. However, PEGylation of nanoparticles, on the other hand, reduce the internalization of cells simultaneously. Therefore, the kinetics of nanoparticles with different PEG density need to be investigated to disclose an optimized PEGylation degree which maintains the benefits of PEGylation as well as a high efficiency of delivery. As illustrated in Figure 2-3C, PEG2-nFLuc, which conjugated with 23 of PEG2000 polymers, exhibited low uptake of nanocapsules with a plateau concentration of 0.15 nM, which could efficiently reduce the phagocytosis. While PEG1-nFLuc with 12 of PEG2000 demonstrated an effective delivery with a plateau concentration of 0.8 nM.

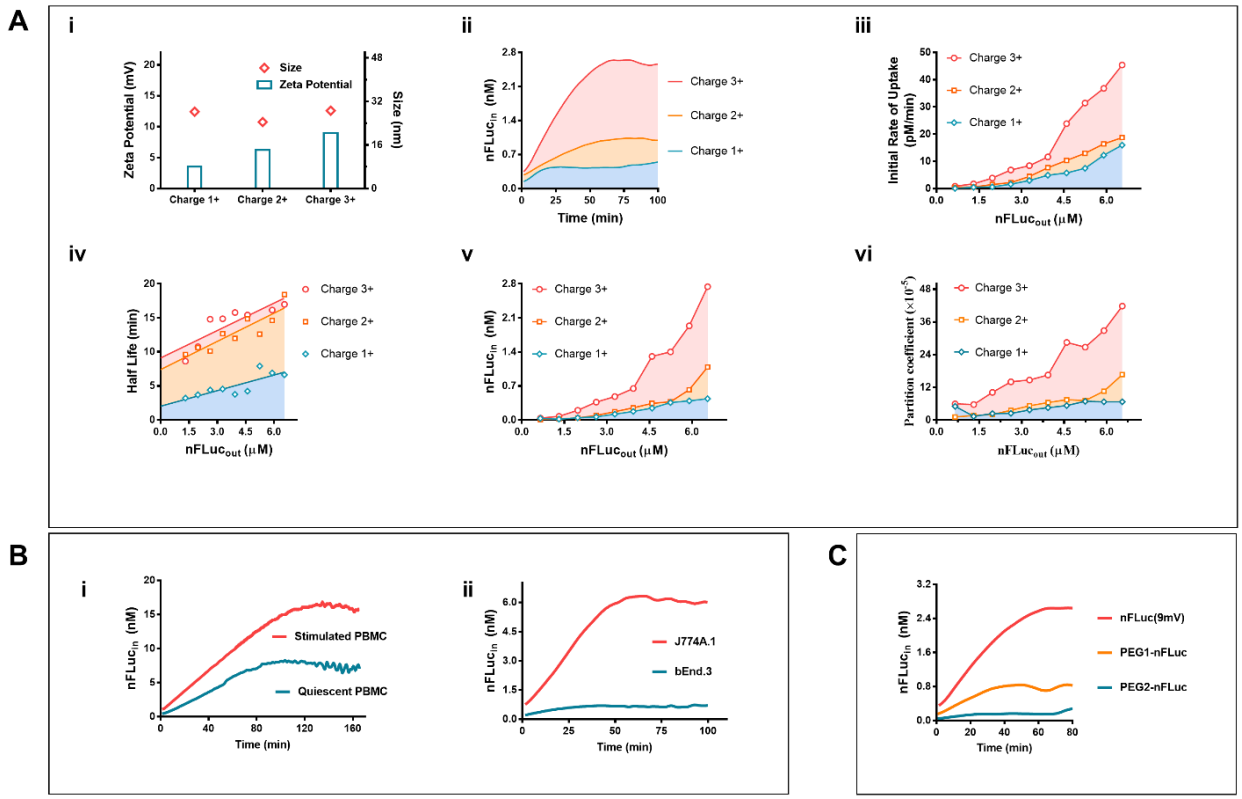

Figure 2-3. Cell internalization kinetics parameters of nFLuc with variable surface charges and PEGylation level in different cells. (A) The internalization kinetics of nFLuc with different surface charges. **(Ai)** Surface charges and sizes of three nFLuc (Charge 1+, Charge 2+, and Charge 3+). **(Aii)** Internalization kinetics of nFLuc with different surface charges in 4T1 cells. **(Aiii)** Initial rates of nFLuc with different surface charges in 4T1 cells. **(Aiv)** Half-lives of nFLuc with different charges in 4T1 cells. **(Av)** The plateau concentration of nFLuc with different charges. **(Avi)** The partition coefficient of nFLuc with different charges when the plateau concentration was reached. **(B)** The internalization kinetics of nFLuc (6mV) in different cells, **(Bi)** in quiescent and stimulated PBMC, **(Bii)** in macrophage cells J774A.1 and brain endothelial cells bEnd3. **(C)** The internalization kinetics of nFLuc(9mV) and PEGylated nFLuc with two ratios of PEG2000 in 4T1 cells.

Besides the enhancement in cell uptake efficiency, the potential for targeting delivery is deemed as another crucial application of nanocapsules. However, there is lack of standard evaluation of targeting efficiency among different cells. To explore an accurate characterization of nanocapsule targeting, the rate of internalization and the efficiency of nanocapsules with targeting ligands are investigated under nFLuc bioluminescence assay. Herein, RGD-nFLuc were adopt as an example to demonstrate the evaluation on targeting efficiency among several cell lines. Meanwhile, nFLuc conjugated with the same density of RAD peptides on the surface, named as RAD-nFLuc, were used as control. The internalization kinetics of three tumor cell lines, 4T1, A549 and Hela with RGD-nFLuc and RAD-nFLuc are compared in Figure 2-4Ai, ii and iii, respectively. The results represented that RGD conjugation increased the internalization rates in all three cell lines. While the targeting efficacy of with RGD conjugation were only increased in A549 and Hela but stayed similarly in 4T1 cells. To delegate internalization capability with nFLuc conjugated various targeting ligands, we defined the equilibrium constant of internalization, K_{eq}, as $K_{eq}=C_{in}/C_{out}$, where C_{in} is the intracellular concentration and extracellular concentration of nFLuc at equilibrium, respectively. Thus, K_{eq} stands for the capability of cell internalization for nFLuc. The targeting efficiency of nFLuc with different ligands can be defined as a dimensionless constant K_{target} as $K_{target}=K_{eq\text{-}target}/K_{eq\text{-}control}$, where $K_{eq\text{-}target}$ is the equilibrium constant of nFLuc with targeting ligand, such as RGD-nFLuc. While $K_{eq\text{-}control}$ is the equilibrium constant of control, RAD-nFLuc for instance. Therefore, K_{target} can be used as a dimensionless parameter for targeting efficiency assessment. K_{target} of nFLuc with a ligand in cells is larger than 1, indicating an improving targeting capability for this specific cell line. Moreover, a larger K_{target} represents a better targeting efficiency. As illustrated in Figure 2-4Aiv, the targeting constant K_{target} of RGD for cell 4T1, A549 and Hela are 0.95, 1.33 and 1.17.

Therefore, RGD is able to efficiently target to both A549 and Hela cells. This assay can evaluate targeting efficiency among different targeting ligands in a vast class of cells for drug screening and precision medicine development.

As a real-time quantitative way to monitor internalization kinetics, this bioluminescent assay provides reliable evaluation and pooled screening for intracellular delivery methods. Cell penetrating peptides (CPPs) are a promising approach to enhance intracellular delivery efficiency. To screen an effective CPP for specific cells, the internalization kinetics of three cell lines (4T1, A549 and Hela) with nFLuc (9mV) conjugated with eight CPPs were investigated, where nFLuc and nFLuc conjugated with one non-penetrating peptide (NPP) were used as negative controls. Eight CPPs, including R10, TAT, Antp, pVEC, NrTP, 14-21, TCTP#35 and PreS2, were conjugated on nFLuc (9mV) surface at an average ratio of 2.3. The plateau concentrations and the initial rates of CPP-conjugated nFLuc in 4T1, A549 and Hela cells were summarized on heat maps and indicated in a color scale (Figure 4B). As showed in Figure 2-4Bi, with CPP conjugation, the plateau concentrations of nFLuc in 4T1 cells were increased 6.43 folds (TCTP#35-nFLuc) to 24.96 folds (R10-nFLuc), while that of nFLuc and NPP-nFLuc showed minimal increase. Among the eight CPPs, R10 and TAT illustrated the highest improvement for cell internalization in all three cell lines. In addition, the initial rates of cell internalization show similar behavior when CPPs were conjugated on nFLuc (Figure 2-4Bii).

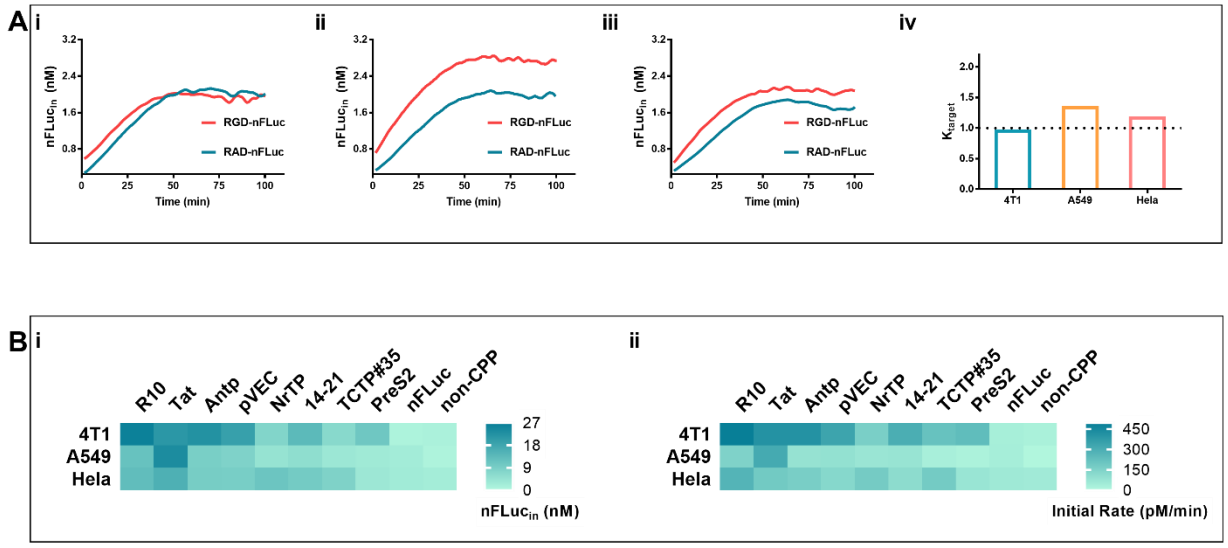

Figure 2-4. Cell internalization kinetics parameters of nFLuc with ligand conjugation. (A) Internalization kinetics of nFLuc conjugation with target ligands (RGD and RAD) in **(Ai)** 4T1, **(Aii)** A549 and **(Aiii)** Hela cells. The RAD-nFLuc was included as negative control. **(Aiv)** Targeting coefficient (K_{target}) of RGD ligands for 4T1, A549 and Hela cells. **(B)** Endocytosis kinetics of nFLuc, CPPs-nFLuc (8 CPPs) and NPP-nFLuc were determined in three cell lines, 4T1, A549 and Hela. The plateau concentrations **(Bi)** and initial rates of cell internalization **(Bii)** were calculated and compared.

2.3 Conclusion

To conclude, we developed a novel system for intracellular protein delivery, RNIKA that enables quantitative and real-time monitoring kinetics of internalization based on FLuc nanocapsules. By realizing precisely spatiotemporal control over distribution and functions, this platform provides a simple and efficient approach for optimization of dosimetry, characterization of therapeutic efficiency and screening of novel medicine. It can be extended to evaluate the

internalization kinetics profiles of other nanostructure-based delivery systems. Therefore, the construction of this bioluminescent assay reveals new hope to evaluate, optimize and predict drug development.

2.4 Experimental Section

2.4.1 Materials

All chemicals were purchased from Sigma-Aldrich unless otherwise noted and were used as received. Recombinant Escherichia coli (E. coli) expressing Firefly luciferase (FLuc) was purchased from Excellgen Corporateion. The nicel-resin affinity column was purchased from Thermo Scientific. Luciferin potassium salt was purchased from Gold Biotechnology. CellTiter-Blue cell viability assay kit was purchased from Promega Corporation. Cell penetrating peptides (CPPs) modified with C-(PEG)2 at N-terminal, c(RGDfC), c(RADfC) were synthetized by ChinaPeptides (Shanghai, China). 4T1, Hela, A549, J774A.1 and bEnd3 cells were purchased from American Type Culture Collection (ATCC). Human PBMCs were obtained without identifying information from the UCLA Center for AIDS Research (CFAR) Virology Core Laboratory in accordance with UCLA Institutional Review Board (IRB) approved protocols along with an IRB-approved written consent form. The Dulbecco's Modified Eagle Medium (DMEM) growth medium, trypsin and Fetal Bovine Serum (FBS) was obtained from Corning.

Table 2-1 Sequences of cell penetrating peptides

name	Peptide Sequence
R10	**RRRRRRRRRR**
TAT	**GRKKRRQRRRP**
Antp	**RQIKIWFQNRRMKWKK**
pVEC	**LLIILRRRIRKQAHAHSK**

14-21	**RLWMRWYSPTARRYG**
TCTP#35	**LIIFAILISHKK**
PreS2	**PLSSIFSRIGDP**
NrTp6	**YKQSHKKGGKKGSG**
nCPP	**WSYGLRPG**

[a] nCPP was predicated from CellPPD

2.4.2 Instruments

UV-Visible spectra were acquired with a Beckman-Coulter DU730. Dynamic light scattering (DLS) studies of the enzyme nanocomplexes was measured on Zetasizer Nano instrument (Malvern Instruments Ltd., Kingdom). Transmission electron microscope (TEM) images were obtained on T12 Quick CryoEM and CryoET (FEI). The bioluminescence intensity and absorbance were measured with a Tecan Infinite 200 PRO plate reader. Fluorescence-activated cell sorting results were achieved by BD LSRFortessa. The fluorescence microscope images were acquired by Leica dmi8 inverted microscope.

2.4.3 Production and purification of FLuc

The fusion proteins were expressed in transformed *E. Coli* Rosetta2 and purified using a nicel-resin affinity column (Thermo Scientific). Bacteria cells were grown in LB medium at 37°C until reaching 0.8 at OD600. The induction of expression was achieved by adding 1mM isopropyl β-D-thiogalactoside (IPTG) at 16°C for 24h. After induction, *E. coli* cells were harvested by centrifugation and resuspended in purification buffer (200 mM NaCl, 50 mM NaH_2PO_4, pH7.4). The FLuc protein were extracted by sonication.

The purification of FLuc proteins were achieved by Ni-NTA column. Briefly, the protein extracts were passed through a Ni-NTA resin column, which was pre-equilibrated with purification buffer. The weakly bound contaminating proteins were washed off by the purification buffer and the washing buffers (20mM and 40mM imidazole in purification buffer). And the His-tagged FLuc proteins were finally eluted with the elusion buffer (250 mM imidazole in purification buffer) and dialyzed against PBS buffer to remove imidazole. To maintain the activity of FLuc, all materials were prechilled in 4°C.

2.4.4 Synthesis of the nanocapsules

2.4.4.1 Acryloxylation of the proteins

Before encapsulation, proteins were first conjugated with acryloyl groups. Acryloxylation of bovine serum albumin (BSA) was achieved by N-acryloxysuccinimide (NAS). Briefly, the BSA proteins were dialyzed against PBS buffer to remove ammonium sulfate in the protein powder. Then, the NAS solution (10% in DMSO, *m/v*) was added to dialyzed BSA solution (10 mg/mL) in ratios of 8:1 at 4 °C for 1 h. And the solution was thoroughly dialyzed against PBS buffer with a dialysis tubing membrane (MWCO= 10 kDa, Sigma-Aldrich).

The average number of acryloyl groups conjugated on BSA proteins surface was further determined by measuring the lysine residues left on the protein by the fluorescamine assay. Briefly, a fresh stock of 3 mg/mL fluorescamine was prepared by dissolving fluorescamine powder in DMSO. And standard was prepared by 2 folds serial dilution of native BSA and acrylolated BSA proteins solution (1mg/mL in PBS) in PBS. Add 25 μL fluorescamine stock solution to 100 μL each assay tube and pipette up and down to mix. Allow the reaction to be

incubated at room temperature for 15 min. After the incubation, the fluorescence intensity (Ex=360 nm, Em=465 nm) was read with a plate reader; and the average number of lysine residues was then estimated by comparing with the standards as 4.5 acryloyl groups onto each BSA proteins.

To avoid activity loss of conjugating with lysine residues at the activity site, the acryloxylation of FLuc enzymes was achieved by conjugating acryloyl groups on cystine residues. Briefly, the reduction of disulfide bonds in FLuc was achieved by incubating the stock solution of FLuc (10 mg/mL in PBS) with 10 mM tris(2-carboxyethyl)phosphine (TCEP) in pH 7.4 at 4 °C for 3 h. Then the stock solution of FLuc was dialyzed against PBS buffer to remove TCEP. And N–(3–aminopropyl) methacrylamide (1% in PBS, *m/v*, APM) was reacted with succinimidyl 4-(N-maleimidomethyl)cyclohexane-1-carboxylate (5% in DMSO, *m/v*, SMCC) with a mole ratio of 1.2:1. Allow the reaction to be incubate at 4 °C overnight until all NHS ester of SMCC reacted. Then, the APM-SMCC solution was added to FLuc stock (10 mg/mL) for acryloxylation with a mole ratio of 10:1. After four-hour incubation at 4 °C, acrylolated FLuc proteins was dialyzed against PBS buffer to remove all unreacted components.

The degree of modification was measured by measuring the cystine residues remained on the FLuc proteins by Ellman's reagent 5,5'-dithio-bis-(2-nitrobenzoic acid) (DTNB). Before the test, the reaction buffer (0.1 M sodium phosphate, pH 8.0, 1mM EDTA0 and Ellman's reagent solution (4 mg/mL DTNB in reaction buffer) were prepared. The standard was then achieved by 2 folds serial dilution of native FLuc and acrylolated FLuc solution (1mg/mL in PBS) in PBS. A set of test tubes, each containing 2 μL of Ellman's reagent solution and 100 μL reaction buffer, were prepared. Added 10 μL of each native or acrylolated FLuc solutions to each test tubes.

Incubated at room temperature for 30 min, the absorbance at 412nm was measured to investigate the average number of acryloyl groups conjugated onto FLuc proteins as 5.0 per FLuc.

2.4.4.2 Synthesis of protein nanoparticles

After acryloxylation, the proteins BSA and FLuc were encapsulated using the *in situ* polymerization method. Reagents for polymerization including acrylamide (AAM) and N-(3-aminopropyl) methacrylamide (APM) were firstly prepared as 30% (*m/v*) and 20% (*m/v*) in PBS for stock solution. And N,N'-methylenebisacrylamide (BIS) as the crosslinker was prepared as 10% (*m/v*) in DMSO. To maintain the activity of FLuc, adenosine triphosphate (ATP) and magnesium sulphate ($MgSO_4$) were prepared as 50 mM in PBS and 100 mM in DI water, respectively. The protein concentration of FLuc and BSA was turned to be 35 μM by diluting with PBS buffer. The proteins were then mixed with the AAM, APM and BIS first with a ratio listed in Table2. Then the polymerization was initiated by adding ammonium persulfate (APS, 10%, *m/v*) and tetramethylethylenediamine (TEMED) and kept at 4 °C for 1 h. After encapsulation, the solution was dialyzed against prechilled PBS buffer to remove unreacted reagents. The details of nFLuc and nBSA nanoparticles were listed in Table 2-2.

Table 2-2 Synthesis parameters of nanoparticles

Sample	Protein	AAM	APM	BIS	APS	TEMED	ATP	$MgSO_4$
nFLuc(0mV)	1	5600	0	500	125	2500	100	100
nFLuc(3mV)	1	5400	200	500	125	2500	100	100
nFLuc(6mV)	1	5200	400	500	125	2500	100	100
nFLuc(9mV)	1	5000	600	500	125	2500	100	100
nFLuc(12mV)	1	4800	800	500	125	2500	100	100
nFLuc(15mV)	1	4600	1000	500	125	2500	100	100
nBSA	1	5400	400	500	125	2500	0	0
nFLuc-Charge 1+	1	5400	200	500	125	2500	100	100
nFLuc-Charge 2+	1	5200	400	500	125	2500	100	100

nFLuc-Charge 3+	1	5000	600	500	125	2500	100	100

2.4.4.3 Conjugation of PEG, RGD, RAD and cell penetrating peptides to nFLuc

To synthesize RGD, RAD and CPP conjugated nFLuc nanoparticles, nFLuc(9mV) was prepared as 3 mg/mL in PBS with ATP and $MgSO_4$ solution. To synthesize PEGylated nFLuc, the nFLuc(9mV) solution was mixed with PEG2000-NHS powder in a mole ratio of 1:20 and 1:40. Then the solution was vortexed to mix and ice bath for 1 hour. To synthesize RGD and CPPs conjugated nFLuc, the succinimidyl 4-(N-maleimidomethyl)cyclohexane-1-carboxylate (SMCC), c(RGDfC), c(RADfC) and CPPs were dissolved in PBS as 10 mg/mL. Then, SMCC solution were added to nFLuc nanoparticles with molar ratio 10:1 at 4 °C for 30 min, followed by dialysis to remove all unreacted SMCC. Then peptides (e.g. c(RGDfC), c(RADfC) and CPPs) were added to nFLuc-SMCC solution with molar ratio of 12:1 at 4 °C for 2 h.

2.4.4.4 Determination of protein concentration

The concentrations of protein nanoparticles, including nFLuc and nBSA, were determined by Pierce™ BCA Protein Assay Kit. Briefly, native protein FLuc or BSA were prepared with a series of enzyme concentrations (1, 0.5, 0.25, 0.125, 0.0625, 0.03125, 0.015625 and 0.0078125 mg/mL). Then, each standard and unknown sample were prepared by mixing 100 μL BCA Reagent A, 2 μL BCA Reagent B and 5 μL sample. Then the mixture was incubated at room temperature for 2 h. Absorbance at 562 nm were measured and compared with the standard curves to calculate the concentration of unknown samples.

2.4.5 TEM and DLS of nanoparticles

TEM samples were prepared as our previous work. Briefly, Drop 2 μL of 0.2 mg/mL nanoparticle solution onto carbon-coated copper grids. After 45s incubation, excess amount of the samples was removed. Then the grid was rinsed with DI water, and stained with 1% sodium phosphotungstate at pH 7.0. To investigate the size and zeta potential of nanoparticles, DLS measurements were taken under the concentration of 0.5 mg/mL.

To confirm the morphology and surface charge of nBSA synthesized with the same procedure of nFLuc(6mV), TEM images and DLS test of nBSA were showed in Figure 2-5.

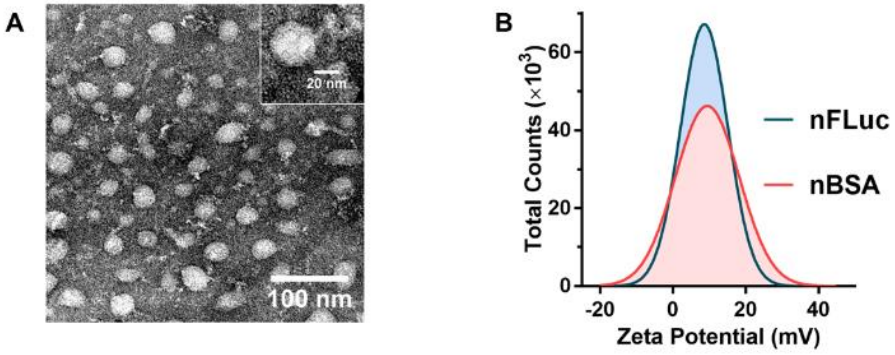

Figure 2-5 Comparison of nBSA and nFLuc. (A) TEM images of BSA nanoparticles encapsulated with the same procedures indicating the same morphology with nFLuc(6mV). **(B)** Comparison of zeta potential of nBSA and nFLuc with the same procedures.

2.4.6 Cell viability test

Cell viability of 4T1, A549 and Hela cells after incubated with nFLuc were investigated at different concentration. Before viability test, 10^4 cells were seeded into a 96-well plate and cultured in 100 μL DMEM medium with 10% FBS and 1% Pen/Strep for a day. Then

nFLuc(6mV) were added into each well with concentrations of 1, 2, 3, 4, 5 μM and incubated with cells for 3 h.

After incubation, CellTilter-Blue (20 μL) was added into each well and further incubated at 37 °C for 3h. Then the fluorescence intensities (Ex=535 nm, Em=585 nm) were quantified with a plate reader. The cell viability results were illustrated in Figure 2-6.

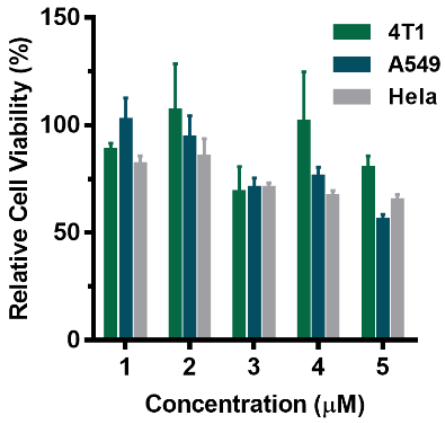

Figure 2-6 Cell viability of 4T1, A549 and Hela cells incubated with different concentration of nFLuc(6mV) nanoparticles.

2.4.7 Fluorescence imaging and fluorescence-activated cell sorting (FACS) test

The cell internalization kinetics were assessed via the fluorescence microscope and fluorescence activated cell sorting (FACS). Hela, A549 and 4T1 cells were cultured in DMEM medium with 10%FBS and 1% penicillin/streptomycin. After 2 days incubation, cells reached 10^4 cells in each well of 96-well plate supplemented with 100 μL medium. Nanocapsules (0.4 mg/mL) were incubated with cells at 37°C for different time. For fluorescence microscopy test,

the cells were rinsed with PBS for three times and fixed with 4% paraformaldehyde for 15 min at room temperature. Then cells were rinsed with PBS and visualized with a fluorescent microscope. For FACS analysis, cells were rinsed with PBS, fixed with paraformaldehyde, trypsinized, centrifuged and re-suspended in PBS and then analyzed with flow cytometry. The fluorescent microscope images of A549 and Hela cells incubated with nFLuc(6mV) and nFLuc(0mV) were showed in Figure 2-7, and the quantification results via FACS were showed in Figure 2-8. Moreover, the cellular uptake quantification of RGD-nFLuc and RAD-nFLuc incubated with 4T1 (Figure 2-9A), Hela (Figure 2-9B) and A549 (Figure 2-9C) were illustrated in Figure 2-9.

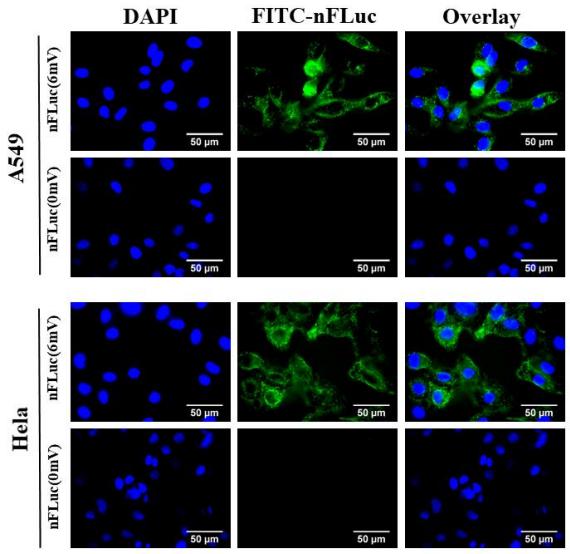

Figure 2-7 Fluorescent images illustrating cell uptake of nFLuc(6mV) and nFLuc(0mV) in A549 and Hela cells.

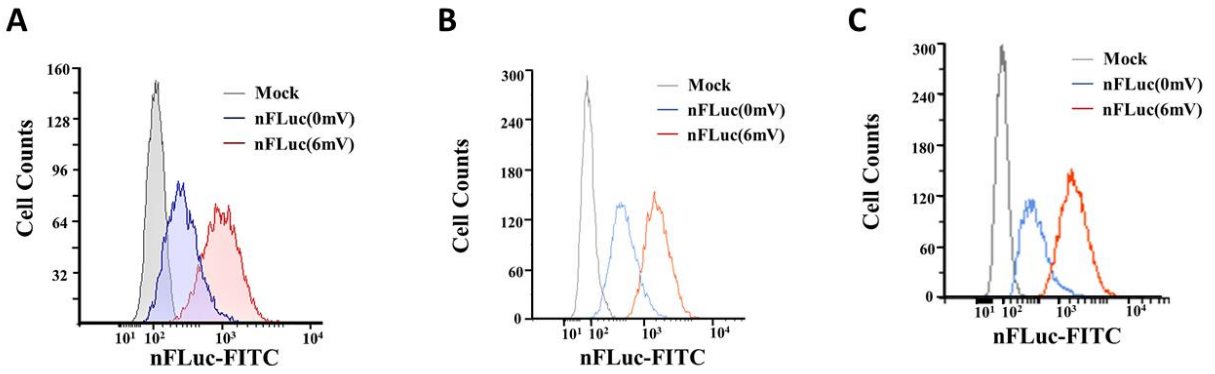

Figure 2-8 Fluorescence-assisted cell sorting of 4T1 cells (A), Hela cells (B) and A549 cells (C) incubated with nFLuc(6mV) and nFLuc(0mV) for 2h at 37 °C.

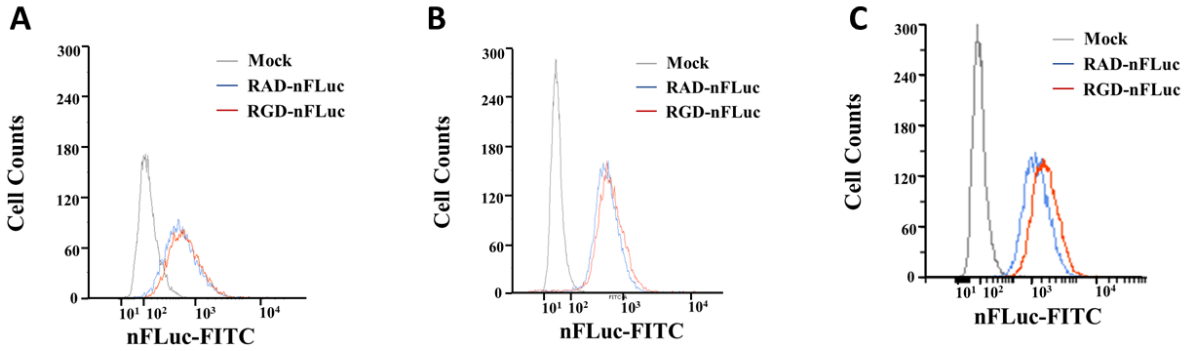

Figure 2-9 Fluorescence-assisted cell sorting of 4T1 cells(A), Hela cells (B) and A549 cells (C) incubated with RGD-nFLuc and RAD-nFLuc for 2h at 37 °C.

2.4.8 Activity assays of nFLuc

The activities of native FLuc and FLuc nanoparticles were assessed by monitoring the rate of bioluminescence reaction. Before the activity test, the substrate buffer was prepared with 20mM tricine, 3.74 mM magnesium sulfate, 0.1mM ethylenediaminetetraacetic acid (EDTA) and

2 mM DTT following by adjusting pH to 7.4. The other stock solutions, including Coenzume A (CoA, 10mM in DI water), ATP (50mM in PBS) and Luciferin (10mM in PBS), were prepared. Then, the activity buffer was prepared by mixing 27μL CoA solution, 10.6 μL ATP solution, 47 μL luciferin solution and 915.5 μL substrate buffer solution. For the tests of bioluminescence reaction rate, 2 μL native FLuc or nFLuc solution (2.5 mg/mL) were added to 35 μL activity buffer in a 96-well plate. And the bioluminescence intensity was monitored by the plate reader with an exposure time setting as 1 s. Compared with native FLuc, nFLuc (6mV) and nFLuc (0mV) remained 82% and 78% of the enzymatic activities, respectively (Figure 2-10).

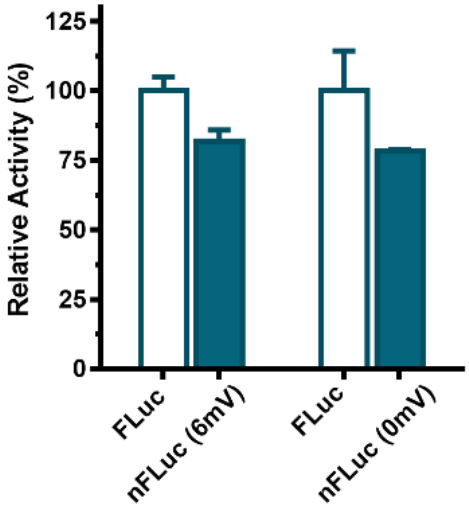

Figure 2-10 Relative activity comparison ofbetween twon FLuc nanoparticles (nFLuc (6mV) and nFLuc (0mV)) and FLuc in native form (FLuc) as control.

2.4.9 Stability assays of FLuc and nFLuc

The stability assays of native FLuc and nFLuc were tested by monitoring the activity of enzymes incubated with PBS and cell lysate at 37 °C. For the stability test in cell lysate. the cell lysate was prepared through the following procedures. The 4T1 cells (10^5 cells) were aspirated and rinsed with PBS buffer. Then the cells were lysed with 200 μL of a cell lysed buffer (Pierce Luciferase Cell Lysis Buffer), scraped from the plate, placed in a 1.5 mL Eppendorf tube and centrifuged to remove the cell debris. The FLuc samples (2.5 mg/mL) were added to the cell lysate with the volume ratio of 1:10. For the stability test in PBS, the FLuc samples (2.5 mg/mL) were directly diluted in PBS with the volume ratio of 1:10. Samples in PBS and cell lysate were then incubated in 37 °C. And the activity of FLuc was tested at different incubation time.

The nFLuc exhibit significant improvement in stability. Figure 2-11 compares the residual activity of nFLuc (6mV) and FLuc at 37 °C in PBS and cell lysate. The half-lives of nFLuc were 92.3 min and 34.5 min in PBS and cell lysate, respectively, approximately 26- and 9- fold longer than those of FLuc. Stability enhancement of nFLuc, especially against low pH and protease degradation in endosome and lysosome, offers advantages on analysis of cellular internalization.

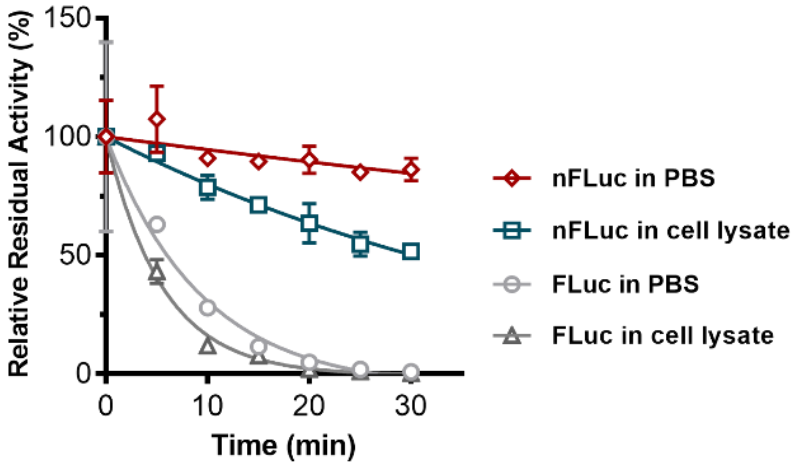

Figure 2-11 Residual enzyme activities of native FLuc and nFLuc (6mV) in PBS and cell lysate at 37℃.

2.4.10 Bioluminescence kinetics measurement of cell internalization

To monitor the bioluminescence kinetics of cell internalization, the luminescence intensity of each single well of a 96-well plate was monitored for 3 h via a Tecan Infinite 200 PRO plate reader. Briefly, 2×10^4 cells were seeded into each well and cultured in 100 μL DMEM medium with 10% FBS and 1% Pen/Strep for a day. The cell culture medium for kinetics test were prepared as DMEM medium without phenol red, with 10% FBS, 1% Pen/Strep and 2mM D-Luciferin potassium salt. Then, we aspired the cell medium, rinsed the cells with PBS buffer and incubated with 100 μL kinetics-test medium for 4 h at 37 °C. After incubation, the cells in 3 of the wells were rinsed with PBS, trypsinized, and counted by hemocytometer as the total cell number N. The cells in the other wells were then rinsed with PBS and incubated with fresh kinetics-test medium to remove the released ATP of dead cells. The exposure time was set as 1

second. The initial time from adding nFLuc samples to the first timepoint measured by the plate reader were monitored with a stopwatch.

2.4.11 Calculation of cell internalization kinetics

To quantify the internalization process, bioluminescence produced each second from a single well of 96-well plates was measured and related to the rate of reaction by Equation (2-1)

$$RLU = \frac{K_{cat}[S]}{K_M+[S]}[nFLuc]e^{-K_d t} \cdot A \cdot N \quad (2\text{-}1)$$

where *RLU* and *N* are the bioluminescent reaction rate with the unit of relative light units per second (RLU/s) and the number of cells in the single well. The measurement procedure of *RLU* and *N* was described as before. To determine the concentration nFLuc, the Michaelis constant K_M, the turnover number k_{cat}, the substrate concentration [*S*], the decay constant K_d, and the conversion factor (RLUs emitted per mole of luciferin reacted) *A* were investigated as below.

2.4.11.1 The Michaelis constant K_M and the turnover number $k_{cat.}$

The Michaelis constant and the turn over number of firefly luciferase were measured via a Lineweaver-Burk plot. The substrate buffer (915.5 μL) mentioned before were firstly mixed with 27μL Coenzyme A (CoA, 10mM in DI water), 10.6 μL ATP (50mM in PBS). Then, a series activity buffers were prepared via adding 47 μL of 10, 5, 2.5, 1.25 and 0.625 mM luciferin solution. The activity of each nFLuc were tested in the series of activity buffers via the procedures described before. And the reciprocal bioluminescence reaction rates were plotted against reciprocal substrate concentrations in the activity buffers of 470, 235, 117.5, 58.75 and

29.375 μM as a linear arrangement. The x-intercept is $-\frac{1}{K_M}$. And the y-intercept is $\frac{A}{k_{cat}\cdot[E]}$. The K_M and k_{cat} of nanoparticles were listed in Table 2-3.

2.4.11.2 The substrate concentration [*S*]

The reaction rate of bioluminescence reaction and the change of substrate concentration can be described as,

$$r = -\frac{\mathrm{d}[\mathrm{S_{in}}]}{\mathrm{d}t} = RLU \cdot \frac{1}{N \cdot A} \tag{2-2}$$

$$\Delta[\mathrm{S_{in}}] = \int_{t_0}^{t_\infty} r\mathrm{d}t = \int_{t_0}^{t_\infty} RLU \cdot \frac{1}{N \cdot A}\mathrm{d}t \tag{2-3}$$

Based on the Equation 2-3, the total concentration changes during the cellular uptake process can be calculated within the range of 1~20 nM, which are much smaller than the initial concentration $[\mathrm{S_{in}}]_0$ (2 mM). Therefore, the profile of substrate concentration inside a cell is allowed to recover by $[\mathrm{S_{in}}]_0$. And the reaction rate can be described as,

$$RLU = \frac{k_{cat}\cdot[\mathrm{S_{in}}]_0}{K_M + [\mathrm{S_{in}}]_0} \cdot [nFLuc] \cdot e^{-K_d t} \cdot N \cdot A \tag{2-4}$$

2.4.11.3 The decay constant K_d

Take the natural logarithm of the both sides in Equation (2-4),

$$\ln RLU = -K_d t + \ln\{\frac{k_{cat}\cdot[S_{in}]_0}{K_M+[S_{in}]_0}\cdot[nFLuc]\cdot N\cdot A\} \quad (2\text{-}5)$$

which indicates that $\ln RLU$ can be described as a linear function of t with a slope of $-K_d$ when the plateau is achieved during cell internalization process. Using the nFLuc(6mV) incubated with 4T1 cells as an example, a line-segment was extracted by the standard Hough transform (red segment, Figure 2-12). And the decay constant of FLuc nanoparticle can be calculated as 1.08×10^{-3} s^{-1}. The K_d nanoparticles were listed in Table 2-3. Accordingly, the concentration of internalized nanoparticles can be calculated as,

$$[nFLuc] = \frac{RLU}{\frac{k_{cat}\cdot[S_{in}]_0}{K_M+[S_{in}]_0}e^{-K_d t}\cdot N\cdot A} \quad (2\text{-}6)$$

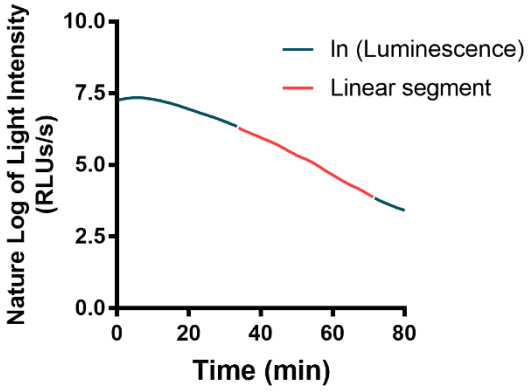

Figure 2-12 The natural logarithm profile of bioluminescence intensity. With the standard hough transform, the decay constant can be calculated the slope of the linear segment (red).

2.4.11.4 The conversion factor *A*

To determine the conversion factor *A*, the turnover number k_{cat} of native FLuc, which was reported as 0.04 s^{-1}, were described as $\frac{A}{k_{cat} \cdot [E]}$. Thus, the conversion factor without cells was calculated to be 3.9 $x10^{11}$ RLU/ (mol oxyluciferin). Considering that light signals obtained from living cells were 68.422 times weaker than that from lysed cells[1], *A* was then determined to be 5.73 $x10^{9}$ RLU/ (mol oxyluciferin).

2.4.11.5 The MATLAB code of the kinetics measurement

```
%% parameters
notation = 'sample';

N = 1.e5;
RLU_in = 5.73e9; % in RLUs/(mol oxyluciferin)
c_luc_in_0 = 2e-3; % in M
K_M = 1.43e-4; % in M
k_cat = 2.3631e-2; % in 1/s
```

```
t_data_whole = xlsread('data.xlsx','sampleName','B22:MF22');
dldt_data_whole_original = xlsread('data.xlsx','sampleName','B23:MF23');

%% smoothing
windowLength = 25; % tunable: 20~30
dldt_data_whole=smoothdata(dldt_data_whole_original,'gaussian',windowLength);

%% searching the probable segement in ln(d[light]/dt)-t plot using Hough
transform
figure;
x = t_data_whole;y = log(dldt_data_whole);
plot(x,y);
axis off;
saveas(gcf,'log.png');close(gcf);

[fitInterval_lb, fitInterval_ub] = HoughTransform('log.png');

%% fitting the segment for estimating rate constant of enzyme decay
startUp = ceil(numel(t_data_whole) * fitInterval_lb) + 1;
cutOff = floor(numel(t_data_whole) * fitInterval_ub);
t_data = t_data_whole(startUp : cutOff);
dldt_data = dldt_data_whole(startUp : cutOff);

[p, s] = polyfit(t_data, log(dldt_data), 1); % linear function
k_d_Fluc = -p(1);

%% estimating update kinetics of enzyme particle
c_luc_in_cal = c_luc_in_0; % reaction consumption is negleted
```

```
c_Fluc_in_cal = dldt_data_whole_original ./ (k_cat * c_luc_in_cal ./ (K_M +
c_luc_in_cal) .* exp(-k_d_Fluc * t_data_whole) * N * RLU_in);

%% generating figure
figure;
set(gcf, 'unit', 'normalized', 'position', [0.2,0.1,0.3,0.8]);

subplot(3, 1, 1);
plot(t_data_whole, dldt_data_whole_original, t_data_whole, dldt_data_whole);
xlabel('time (s)'); ylabel('reaction luminesecence');
title(['experimental data: ' notation]);
axis([0 max(t_data_whole) 0 1.2 * max(dldt_data_whole)]);
legend('original', ['smoothed (Gaussian:' num2str(windowLength) ')']);

subplot(3, 1, 2);
plot(t_data_whole, log(dldt_data_whole), t_data, log(dldt_data), t_data,
(t_data * p(1) + p(2)));
xlabel('time (s)'); ylabel('{\itnatural logarithm} of reaction
luminesecence');
title(['linear regression on [', num2str(fitInterval_lb), ', ',
num2str(fitInterval_ub), ']: k_{decay} = ', num2str(-p(1)) ' s^{-1}']);
axis([0 max(t_data_whole) 0 1.2 * max(log(dldt_data_whole))]);
legend('whole course', 'truncated', 'truncated (fitted)');

subplot(3, 1, 3);
h3=plot(t_data_whole / 60, c_Fluc_in_cal * 1e9); % convert units
xlabel('time (min)'); ylabel('[P_{in}] (nM)');
title('calculated enzyme particle uptake kinetics');
axis([0 max(t_data_whole) / 60 0 1.2 * max(c_Fluc_in_cal * 1e9)]);
```

```
saveas(gcf,[notation '.tif']);%close (gcf);


%% generating Microsoft Excel sheet
parameterList={'quantity','unit','value','method';...
    'k_cat','1/s',k_cat,'experiment';...
    'K_M','M',K_M,'experiment';...
    '[S_in]','M',c_luc_in_0,'experiment';...
    'N','1',N,'experiment';...
    'luminescence intensity','RLUs/mol',RLU_in,'experiment';...
    'k_d.nFluc','1/s',k_d_Fluc,['fitting: [', num2str(fitInterval_lb), ',',
num2str(fitInterval_ub), ']']};
outputTitle={'t (min)',...
    'luminescence intensity ',...
    'luminescence intensity (smoothed)',...
    'natural logarithm of light intensity ',...
    'estimated internal enzyme particle concentration (nM)'};
outputData=[t_data_whole'/60,...
    dldt_data_whole_original',...
    dldt_data_whole',...
    log(dldt_data_whole)',...
    c_Fluc_in_cal'*1e9];


xlswrite('MATLABoutput.xlsx', parameterList, notation, 'A1');
xlswrite('MATLABoutput.xlsx', outputTitle, notation, 'G1');
xlswrite('MATLABoutput.xlsx', outputData, notation, 'G2');


%% help function for Hough transform
function [interval_lb, interval_ub]= HoughTransform(figName)
```

```
% SOURCE:
% http://blog.csdn.net/yangpan011/article/details/53644579

I = imread(figName);%I=imread('conc.png');
Ihsv = rgb2hsv(I);
Iv = Ihsv(:,:,3);
Ivl = Iv(1:end,:);
Iedge = edge(Ivl,'sobel');
Iedge = imdilate(Iedge,ones(3));

figure;
imshow(Iedge);
hold on;

[H1,T1,R1] = hough(Iedge, 'Theta', -90:1:89);
Peaks = houghpeaks(H1, 1);%'Threshold',0.5);

lines = houghlines(Iedge, T1, R1, Peaks);
X_1_fit_lb = lines(1).point1(1); X_1_fit_ub = lines(end).point2(1);

for k=1:length(lines)
    xy = [lines(k).point1; lines(k).point2];
    plot(xy(:,1), xy(:,2), 'LineWidth', 2);
end

[Y_1,X_1] = find(Iedge == 1);
X_1_lt = X_1(1); X_1_rt = X_1(end);
hold all;
scatter([X_1(1), X_1(end)],[Y_1(1), Y_1(end)]);
```

```
interval_lb = (X_1_fit_lb - X_1_lt) / (X_1_rt - X_1_lt);

interval_ub = (X_1_fit_ub - X_1_lt) / (X_1_rt - X_1_lt);


end
```

2.4.12 Summary of nFLuc parameters for kinetics calculation

The parameters of different FLuc nanoparticles were summarized in Table 2-3.

Table 2-3. Parameters of nanoparticles kinetics calculation.

Nanoparticle	Cell	K_M (M)	k_{cat} (s^{-1})	N	K_d (s^{-1})	Linear Segment	
						Start (min)	End (min)
nFLuc(6mV)	PBMC stimulated	0.0012	0.0310	120000	0.00064	102.29	174.85
nFLuc(6mV)	PBMC quiescent	0.0012	0.0310	120000	0.00087	77.72	144.80
nFLuc(6mV)	J774A.1	0.0012	0.0310	80000	0.00092	45.62	120.68
nFLuc(6mV)	bEnd3	0.0012	0.0310	140000	0.00100	29.46	98.79
nFLuc(3mV)	4T1	0.00012	0.0220	100000	0.00062	23.36	40.94
nFLuc(3mV)	4T1	0.00012	0.0220	100000	0.00064	15.07	43.38
nFLuc(3mV)	4T1	0.00012	0.0220	100000	0.00071	16.53	61.44
nFLuc(3mV)	4T1	0.00012	0.0220	100000	0.00066	17.51	66.32
nFLuc(3mV)	4T1	0.00012	0.0220	100000	0.00067	19.46	82.42
nFLuc(3mV)	4T1	0.00012	0.0220	100000	0.00067	17.99	72.17
nFLuc(3mV)	4T1	0.00012	0.0220	100000	0.00064	18.97	80.96
nFLuc(3mV)	4T1	0.00012	0.0220	100000	0.00061	27.76	83.89
nFLuc(3mV)	4T1	0.00012	0.0220	100000	0.00065	20.43	79.49
nFLuc(3mV)	4T1	0.00012	0.0220	100000	0.00062	18.97	75.59
nFLuc(6mV)	4T1	0.00014	0.0240	100000	0.00031	20.47	81.10
nFLuc(6mV)	4T1	0.00014	0.0240	100000	0.00041	21.94	68.39
nFLuc(6mV)	4T1	0.00014	0.0240	100000	0.00043	34.16	93.85
nFLuc(6mV)	4T1	0.00014	0.0240	100000	0.00052	37.10	101.67
nFLuc(6mV)	4T1	0.00014	0.0240	100000	0.00052	41.98	119.76
nFLuc(6mV)	4T1	0.00014	0.0240	100000	0.00051	37.58	89.94

nFLuc(6mV)	4T1	0.00014	0.0240	100000	0.00059	47.36	103.14
nFLuc(6mV)	4T1	0.00014	0.0240	100000	0.00051	42.47	86.03
nFLuc(6mV)	4T1	0.00014	0.0240	100000	0.00049	53.72	125.63
nFLuc(6mV)	4T1	0.00014	0.0240	100000	0.00047	60.07	135.41
nFLuc(9mV)	4T1	0.00016	0.0240	100000	0.00045	33.67	94.83
nFLuc(9mV)	4T1	0.00016	0.0240	100000	0.00048	33.18	108.03
nFLuc(9mV)	4T1	0.00016	0.0240	100000	0.00056	42.47	104.61
nFLuc(9mV)	4T1	0.00016	0.0240	100000	0.00057	53.23	120.25
nFLuc(9mV)	4T1	0.00016	0.0240	100000	0.00054	48.83	125.14
nFLuc(9mV)	4T1	0.00016	0.0240	100000	0.00054	49.32	115.85
nFLuc(9mV)	4T1	0.00016	0.0240	100000	0.00061	53.23	128.07
nFLuc(9mV)	4T1	0.00016	0.0240	100000	0.00058	43.94	126.12
nFLuc(9mV)	4T1	0.00016	0.0240	100000	0.00060	53.72	123.67
nFLuc(9mV)	4T1	0.00016	0.0240	100000	0.00062	55.19	114.87
RGD-nFLuc	A549	0.00078	0.0130	100000	0.00073	44.19	120.70
RGD-nFLuc	Hela	0.00078	0.0130	125000	0.00080	40.24	112.44
RGD-nFLuc	4T1	0.00078	0.0130	110000	0.00081	37.73	109.21
RAD-nFLuc	A549	0.00079	0.0130	100000	0.00084	46.14	100.74
RAD-nFLuc	Hela	0.00079	0.0130	125000	0.00079	45.62	123.31
RAD-nFLuc	4T1	0.00079	0.0130	110000	0.00091	45.62	104.41
R10-nFLuc	4T1	0.00012	0.0040	100000	0.00084	73.28	159.88
R10-nFLuc	Hela	0.00028	0.0013	108300	0.00069	64.13	147.86
R10-nFLuc	A549	0.00017	0.0005	177500	0.00069	64.49	124.60
TAT-nFLuc	4T1	0.00038	0.0057	100000	0.00089	62.25	147.47
TAT-nFLuc	Hela	0.00096	0.0191	108300	0.00074	85.26	181.41
TAT-nFLuc	A549	0.00062	0.0006	177500	0.00064	70.90	136.43
Antp-nFLuc	4T1	0.00035	0.0205	100000	0.00101	52.59	140.02
Antp-nFLuc	Hela	0.00014	0.0008	108300	0.00059	69.41	155.26
Antp-nFLuc	A549	0.00163	0.0019	177500	0.00059	94.55	155.89
pVEC-nFLuc	4T1	0.00073	0.0052	100000	0.00080	71.35	158.23
pVEC-nFLuc	Hela	0.00042	0.0015	108300	0.00058	83.67	161.08
pVEC-nFLuc	A549	0.00078	0.0008	177500	0.00056	78.53	130.27
NrTp	4T1	0.00075	0.0049	100000	0.00086	58.66	133.40
NrTp	Hela	0.00023	0.0030	108300	0.00073	75.48	148.13
NrTp	A549	0.00026	0.0004	177500	0.00044	66.46	174.37
14-21-nFLuc	4T1	0.00034	0.0041	100000	0.00083	69.69	147.47
14-21-nFLuc	Hela	0.00173	0.0497	108300	0.00090	72.05	157.91
14-21-nFLuc	A549	0.00042	0.0007	177500	0.00055	69.17	149.73
TCTP#35-nFLuc	4T1	0.00012	0.0014	100000	0.00096	37.98	102.79
TCTP#35-nFLuc	Hela	0.00016	0.0009	108300	0.00070	62.01	129.11
TCTP#35-nFLuc	A549	0.00043	0.0071	177500	0.00069	82.97	156.87
PreS2-nFLuc	4T1	0.00037	0.0131	100000	0.00101	47.35	142.50
PreS2-nFLuc	Hela	0.00032	0.0031	108300	0.00070	58.31	144.17

PreS2-nFLuc	A549	0.00072	0.0110	177500	0.00069	83.21	154.66
nFLuc	4T1	0.00413	0.0875	100000	0.00115	30.53	104.99
nFLuc	Hela	0.00036	0.0049	108300	0.00082	54.09	122.24
nFLuc	A549	0.00013	0.0015	177500	0.00062	60.06	128.54
ncpp-nFLuc	4T1	0.00998	0.2781	100000	0.00107	47.63	113.82
ncpp-nFLuc	Hela	0.00077	0.0019	108300	0.00061	62.54	126.20
ncpp-nFLuc	A549	0.00021	0.0296	177500	0.00068	83.71	161.56

Chapter 3. Zwitterionic firefly luciferase nanocapsules for cancer diagnosis

3.1 Introduction

Cancer becomes a major public health problem in the United States and many other parts all over the world during the past decades. According to the statistics data provided by the American Cancer Society, there are 1,665,540 new cancer cases diagnose in 2014, equivalent of more than 4,500 cases each day. Cancer had become the second leading cause of death following heart disease, which caused 574,743 (23%) deaths in a total of 2,468,435 recorded in the United States in 2010[116]. It can be distressing not just for person concerned, but for national public health institutes as well. The National Institutes of Health(NIH) estimated that the overall costs, including direct medical expenditures and indirect mortality costs17, were $216.6 billion in 2009[117]. Yet today, effective diagnoses and treatments remain an international quagmire and deserve nothing less than our most tenuous efforts. Techniques such as magnetic resonance imaging (MRI), x-ray computed tomography (CT) nuclear imaging, optical imaging and ultrasound are likely to revolutionize the way we detect and monitor cancer[118,119]. Despite the recent advances in cancer research techniques, we are still limited in real-time visualization of tumor, especially in the early stage[120].

Recent studies show that pathological situations such as tumors may lead to large increases in extracellular concentration of adenosine-5'-triphosphate (ATP), which is the most commonly used phosphate donor. It would be a potential approach for cancer diagnosis via detection of extracellular ATP concentration[121–124]. Several methods have been developed to quantify extracellular ATP. The firefly luciferase (FLuc) assay which is super sensitive for

quantitation of ATP is one of the most widely applied methods. However, most studies are depended on transgenically modified tumor cells due to the poor stability of FLuc. For instance, Patrizia and coworkers successfully developed a chimeric plasma membrane-targeted method, which could anchor luciferase to the tumor cell membrane, to detect the concentration of extracellular ATP in the tumour site[125,126]. Their results indicate that ATP in the tumour interstitium is in the hundrends micromolar range, while it is basically undetectable in healthy tissues. But, the safety concerns caused by transgenically modified tumor cells and the errors brought by luciferases location limit the application of this method, especially in clinic settings.

We herein report a novel approach for cancer diagnosis based on FLuc nanocapsules, which are sensitive to the extracellular ATP concentration. This nanocapsule was achieved by conjugating the polymerizable acryloyl groups on native FLuc molecules. The FLuc with acryloyl groups was then mixed with 2-methacryloyloxyethyl phosphorylcholine (MPC) as monomer and the N,N'-methylenebisacrylamide (BIS) as the crosslinker (Figure 3-1, Step I). The monomers and crosslinkers will be enriched on the protein surface due to the noncovalent interactions and subsequently form a thin layer of polymer shell via in situ polymerization around the native protein surface (Figure 3-1, Step II). Such polymer shell allows an efficient transport luciferin and ATP for the bioluminescence reaction. Moreover, endowed with zwitterionic polymer PMPC, the FLuc nanocapsules with stealth surface can improve the stability and prolong the retention time in plasma (Figure 3-1, Step III). The increased extracellular ATP concentration at tumor site enables FLuc to catalyze bioluminescence reaction for cancer diagnosis (Figure 3-1, Step IV). This FLuc nanocapsules with a FLuc protein core inside and PMPC polymer outside is denoted as PMPC-nFLuc, where the prefix 'n' represents for the nanocapsule.

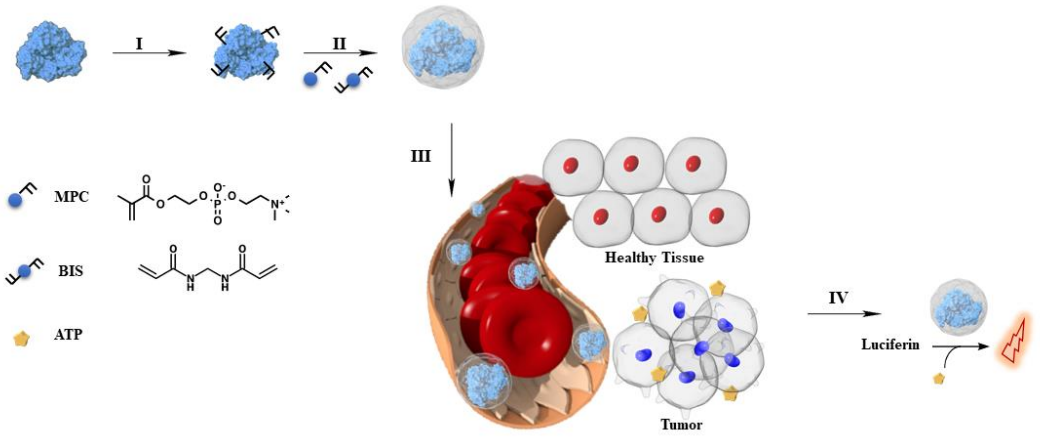

Figure 3-1 Schematic illustration of the synthesis of PMPC-nFLuc nanocapsules and light emission on the tumor site. Synthesis of the PMPC-nFLuc nanocapsules are achieved by **Step I,** conjugate of the FLuc with acryloyl groups. **Step II,** mixe FLuc with 2-methacryloyloxyethyl phosphorylcholine (MPC) as monomer and the N,N'-methylenebisacrylamide (BIS) as the crosslinker and initiate in situ polymerization to form a thin layer of polymer around the native protein surface. **Step III**, intravenously inject PMPC-nFLuc nanocapsules. Endowed with zwitterionic polymer PMPC, the FLuc nanocapsules with stealth surface can improve the stability and prolong the retention time in plasma. And **Step IV**, when reaching the tumor site, the increased extracellular ATP concentration enables FLuc to catalyze bioluminescence reaction for cancer diagnosis.

3.2 Results and discussion

The successful encapsulation of native FLuc was investigated by monitoring the morphology of PMPC-nFLuc via transmission electron microscopy (TEM). As illustrated in Figure 3-2A, the PMPC-nFLuc nanocapsules exhibited a spherical morphology with an average

diameter of about 25 nm. The size distribution of PMPC-nFLuc achieved by the dynamic light scattering confirmed this result (Figure 3-2B). After encapsulation, the size of PMPC-nFLuc increased from 7 nm of the native FLuc to 25 nm, suggesting a 9-nm-thick of PMPC polymer shell wrapped on native FLuc. Moreover, the zeta potential of the PMPC-nFLuc nanocapsules were altered to 0 mV from -9 mV of native FLuc, demonstrating a full coverage of PMPC polymers around FLuc molecules (Figure 3-2C).

To investigate the influence of the PMPC charge and stealing properties on its behavior, another two FLuc nanocapulse, PAAM-nFLuc and PAPM nFLuc, were synthesized by altering the monomers to acrylamide (AAM, a neutral charged non-zwitterionic monomer) and the mixture of AAM with positively charged monomer N-(3-Aminopropyl) methacrylamide hydrochloride (APm). The PAAM-nFLuc nanocapsules exhibited the same neutral charged surface as PMPC-nFLucs. Whereas the PAPM-nFLuc nanocapsules was assessed as a positively charged surface in 10 mV. Worth noting that, all these three nanocapsules were in the size as 25 nm in diameter, which eliminating the size effect.

The majority of enzymatic activity of FLuc was retained after encapsulation. Figure 3-2D compared the residual activity of native FLuc with the nFLuc nanocapsules encapsulated with PAPM, PAAM and PMPC, showing that more than 84 % of the enzymatic activity retained after encapsulation. In addition, the capability of nFLuc nanocapsules as a ATP indicator was assessed by monitoring the luminescence intensity produced under a series ATP concentration. The range of ATP concentration was fluctuating form 0.05 μM to 100 μM to mimicking the extracellular ATP concentration in the health tissues and tumor site. As shown in Figure 3-2E, the luminescence intensity emitted by both native FLuc and PMPC-nFLuc revealed a linear

progression when ATP concentration arise with a slope of 48.4 and 43.2 counts/μM, respectively. This result revealed that the encapsulation process had no influence on the sensitivity of FLuc.

The cytotoxicity of PMPC-nFLuc was investigated by CellTiter-Blue cell viability assays. The 4T1 cells were incubated with a series concentration of PMPC-nFLuc nanocapsules ranging from 200 nM to 1200 nM at 37 °C for 24 h. The corresponding native FLuc was adopt as control. Normalized by the 4T1 cells incubated with PBS buffer, about 100 % of the cell viability maintained exposed to PMPC-nFLuc treatment.

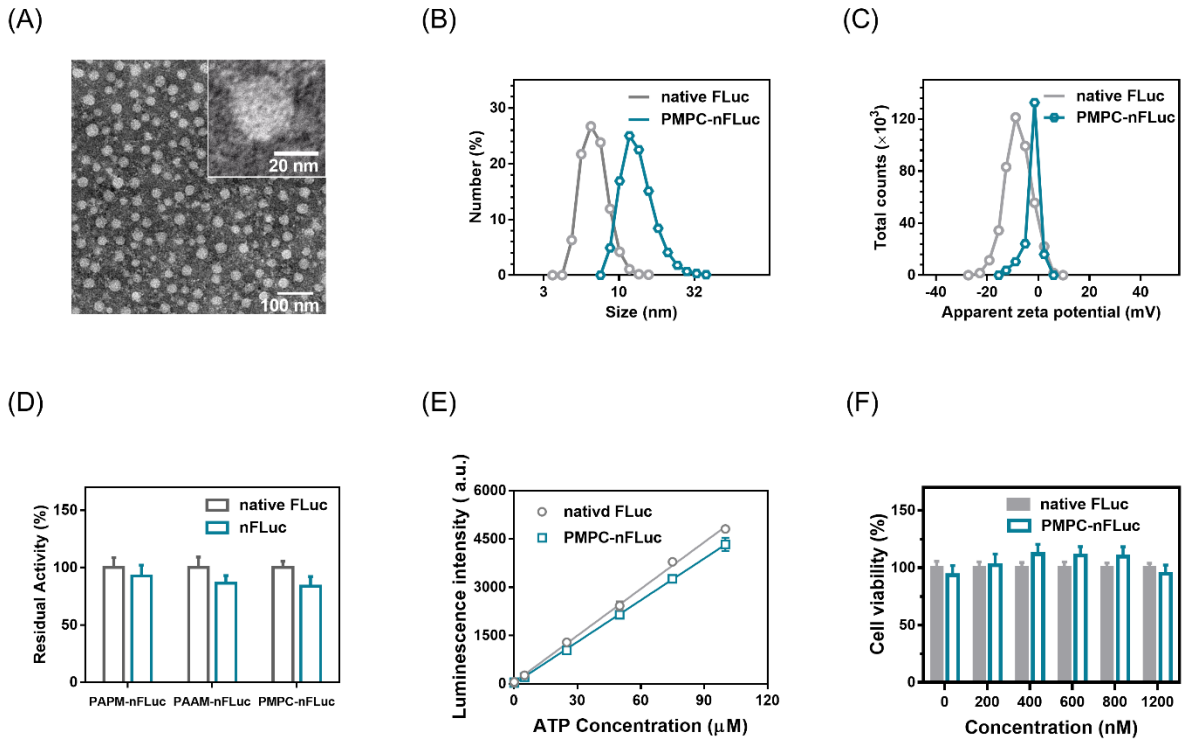

Figure 3-2 Characterization of morphology, size distribution, zeta potential, activity, ATP sensitivity and cytotoxicity of nanocapsules. (A) TEM images of PMPC-nFLuc nanocapsules, which reveals a uniformed sphere with the size of 25 nm in diameter. **(B)** The size distribution of native FLuc and PMPC-nFLuc achieved by DLS. **(C)** The zeta potential distribution of native FLuc and PMPC-nFLuc. **(D)** Residual enzyme activity of PAPM-nFLuc, PAAM-nFLuc, PMPC-nFLuc after encapsulation. Data present by mean ± standard derivation (s.d.), n=3. **(E)** Bioluminescence intensity produced by catalysis reaction of native FLuc and PMPC-nFLuc nanocapsules with different ATP concentrations. Data present by mean ± standard derivation (s.d.), n=3. **(F)** The CellTiter-Blue cell viability assays after incubation with native FLuc and PMPC-nFLuc for 24 hours. Data present by mean ± standard derivation (s.d.), n=3.

Despite of the broad application in bioluminescence imaging as genetic reporters, the poor stability of FLuc restricts its utility as probe molecules. Our nFLuc nanocapsules can improve stability against thermal denaturation and proteolysis. Figure 3-3A demonstrated the residual activity of native FLuc and PMPC-nFLuc in 37 °C. The native FLuc lost almost of all the activity after 40-min incubation, whereas PMPC-nFLuc retained more than 90 % of the enzymatic activity after 40 min (Figure 3-3A). In addition, the PMPC polymer shells evade a degradation of the protease. Using trypsin as an example, the residual activity of the PMPC-nFLuc and native FLuc were monitored by incubating with 0.1 mg/mL trypsin. As illustrated in Figure 3-3A, the activity of native FLuc diminished to 0 after 20 min incubation. While PMPC-nFLuc nanocapsules, on the other hand, remained 70 % activity after 40 min. The improvement of FLuc stability offers a huge advantage on its in vivo utility against proteas degradation.

The stability of the nFLuc nanocapsules in mouse serum is further evaluated. Samples (1 mg/mL) including native FLuc and PMPC-nFLucs, PAAM-nFLuc, PAPM-nFLuc were mixed with 50 mg/mL mouse serum and incubated at 37 °C for 4 hours. Mouse serum incubated with PBS buffer was used as control. After incubation, the mixture was evaluated by DLS. As illustrate in Figure 3-3B, the PBS control samples exhibited 6 nm size since the main components of mouse serum are proteins with a size less than 10 nm. The PMPC-nFLuc revealed the similar size distribution, suggesting that there was no obvious aggregation incubated with the serum. Whereas the native FLuc, PAAM-nFLuc, and PAPM-nFLuc demonstrated 12 nm, 14 nm and 24 nm size after serum incubation, because of the unstable nature, relative hydrophobic surface and the positive charge.

Besides the enhance of stability, the ability of PMPC-nFLuc nanocapsules to evade immune clearance, such as phagocytosis and opsonization, was illustrated by cell internalization analysis of the mouse macrophage cells J774A.1. The rhodamine B labelled native FLuc and nFLuc nanocapsules were pre-incubated with mouse serum in 37 °C for 3 hours allowing the samples to be opsonized before exposed to the J774A.1 cells for 2 h incubation. The macrophages were then detected under the fluorescence microscope. As expected, the J774A.1 cells treated with PAPM-nFLuc were intensely fluorescent since the positively charged surface. Yet the J774A.1 cells incubated with native FLuc and PAAM-nFLuc were fluorescent as well, demonstrating that the opsonized native FLuc and PAAM-nFLuc will induce phagocytosis. The PMPC-nFLuc treated cells, on the other hand, showed little phagocytosis (Figure 3-3C). The fluorescence intensity of J774A.1 cells was further quantified by the fluorescence-activated cell sorting (FACS) analysis. Consistent with the fluorescence microscope results, the PMPC-nFLuc treated cells demonstrated the similar level of fluorescence with the mock. While the cells

incubated with the native FLuc, PAAM-nFLuc or PAPM-nFLuc reveals more than 10 folds higher fluorescence intensity (Figure 3-3D).

The capability of PMPC polymer shells to diminish the opsonization by serum proteins were confirmed by quantifying the protein adsorption. After 1 h incubated with mouse serum, the mixture of PMPC-nFLuc and mouse serum were filtered by 30 kD filter. The proteins with the molecular weight larger than 30 kD were quantified as adsorbed proteins. As shown in Figure 3-3E, the native FLuc, PAAM-nFLuc and PAPM-nFLuc exhibited significant protein adsorption, whereas PMPC-nFLuce demonstrated no evidence of protein adsorption. Therefore, the FLuc covered with the zwitterionic PMPC polymer can efficiently prevent the opsonization and phagocytosis.

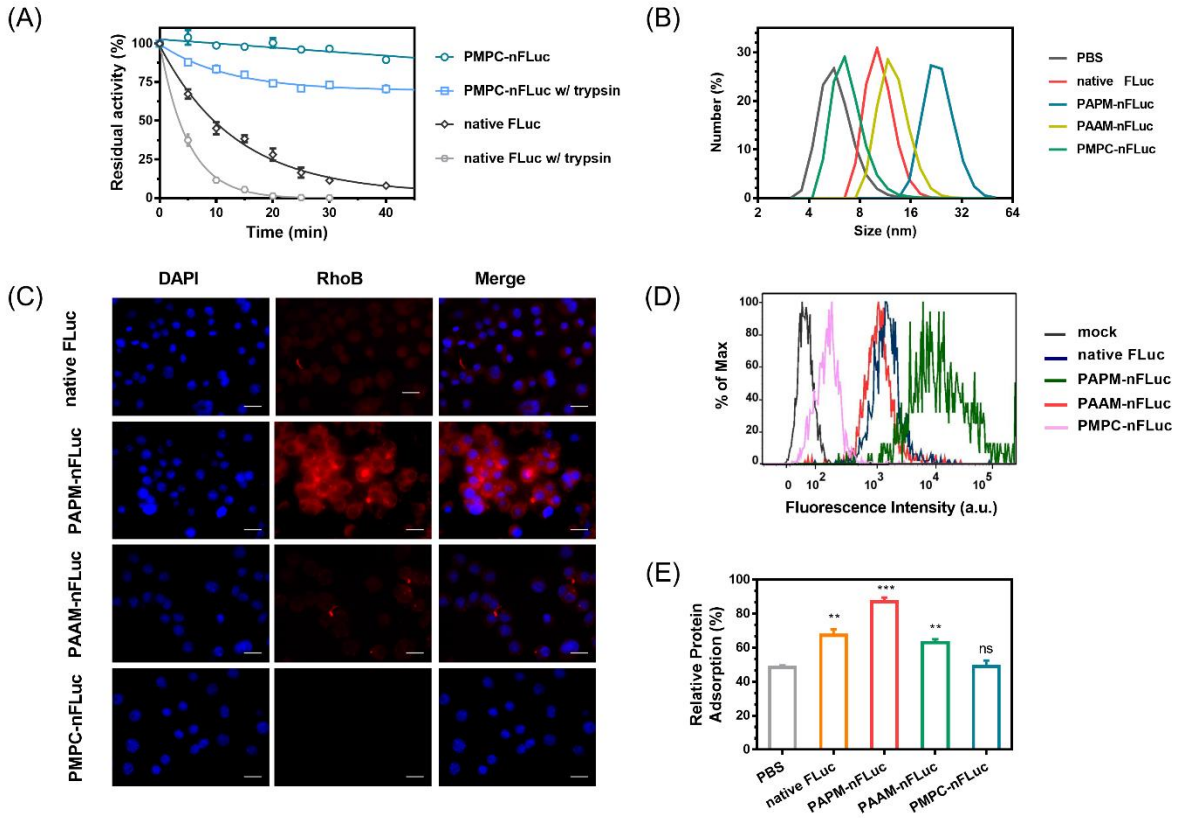

Figure 3-3 Characterization of stability, phagocytosis, and protein adsorption of nanocapsules. (A) Relative residual activity of native FLuc and PMPC-nFLuc with and without 0.1 mg/mL trypsin after incubation at 37 °C. Data present by mean ± standard derivation (s.d.), n=3. **(B)** Size distribution results of native FLuc and PMPC-nFLucs, PAAM-nFLuc, PAPM-nFLuc after incubation with mouse serum at 37 °C for 4 hours. Mouse serum incubated with PBS buffer was used as control. **(C)** Fluorescence images of J774A.1 mouse macrophage uptake of Rhodamine B labelled native FLuc and PMPC-nFLucs, PAAM-nFLuc, PAPM-nFLuc nanocapsules after incubation for 2 h at 37 °C. The samples were pre-incubated with mouse serum in 37 °C for 1 hours. **(D)** Fluorescence-assisted cell sorting (FACS) analysis of the J774A.1 mouse macrophages at 3 hours post incubation with native FLuc and nFLucs in 37 °C.

(E) Percentage of protein adopted on the native FLuc, PMPC-nFLucs, PAAM-nFLuc, PAPM-nFLuc nanocapsules after incubated with mouse serum in 37 °C for 1 hour. Data present by mean ± standard derivation (s.d.), n=3.

The improved stability and reduce immune clearance allows the PMPC-nFLuc to serve as a probe for ATP mapping. The ability of bioluminescence imaging of PMPC-nFLuc was first assessed by subcutaneous administration. The optical imaging results exhibit bioluminescence produced by subcutaneously injected native FLuc at the left site and PMPC-nFLuc at the right site in the same mouse. As illustrated in Figure 3-4A, both native FLuc and PMPC-nFLuc exhibited light emission after 15 min post subcutaneous injection. However, the luminescence intensity produced by PMPC-nFLuc was much stronger then the native FLuc. In addition, signal of the native FLuc disappeared at 24 h post injection. While the luminescent signals of PMPC-nFLuc lasted as long as 48 h. The luminescence intensity at the injection site was quantified in Figure 3-4B, the luminescent intensity of PMPC-nFLuc was 12 folds and 27 folds higher than native FLuc at 15 min and 24 h post injection.

The pharmacokinetics profile of PMPC-nFLuc was investigated by intravenous inject the PMPC-nFLuc nanocapsules with the native FLuc as control. To quantify the concentration in the plasma, the activity of FLuc were measured at various time post injection. Figure 3-4C reveals the plasma concentration of mice treated with PMPC-nFLuc and native FLuc. The native FLuc exhibited little concentration in mouse plasma after 15 min. Compared with the native FLuc, PMPC-nFLuc nanocapsules maintained significantly higher plasma concentration with a 14 h half-life. The prolonged circulation time improved the bioavailability of PMPC-nFLuc in the

organs, allowing the nanocapsules to circulate around the whole body for cancer diagnosis purposes.

The capability of PMPC-nFLuc to detect tumor was examined in mice bearing 4T1 xenograft tumor. Figure 3-4D depicted the optical imaging results obtained from the PMPC-nFLuc intravenously injected to the mouse bearing xenograft tumor at second mammary gland (blue arrow). The clear luminescence signal colocalized at the tumor site indicated the tumor could be diagnosed by PMPC-nFLuc nanocapsules with high specificity. The luminescence signals at the tumor site were further quantified and compared with the native FLuc (Figure 3-4E). The native FLuc showed litter luminescence emitted at the tumor site through 48 h post injection. While the PMPC-nFLuc showed intensely luminescent especially at 16 h post injection.

Quantification analysis of the main organs distribution in the mice bearing xenograft tumor was conducted at 16 h post PMPC-nFLuc and native FLuc injection. As illustrated in Figure 3-4F the little luminescence was emitted by the organs of mice treated with native FLuc. In addition, an obvious accumulation in liver was observed after treated with native FLuc. The PMPC-nFLuc nanocapsules, however, demonstrated a high specificity in the tumor.

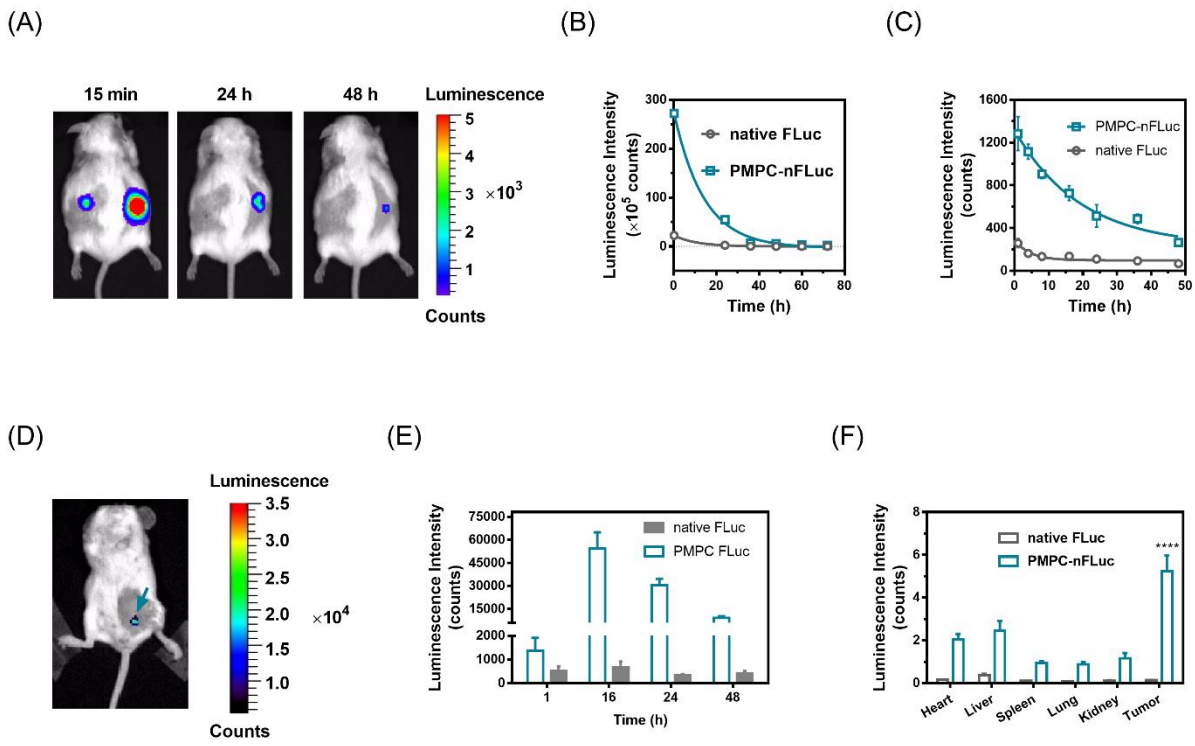

Figure 3-4 Characterization of in vivo stability, pharmacokinetics profiles, tumor diagnosis and biodistribution of PMPC-nFLuc nanocapsules. (A) Bioluminescence images of mouse administered with native FLuc (left site) and PMPC-nFLuc (right site) at 15 min, 24 h and 48 h post subcutaneous injection. **(B)** Luminescence intensity quantification of native FLuc and PMPC-nFLuc in mice at 15 min, 24 h, 36 h, 48 h, 60 h and 72 h post subcutaneous injection. Data present by mean ± standard derivation (s.d.), n=3. **(C)** Pharmacokinetic profiles of native FLuc and PMPC-nFLuc in mouse plasma post intravenous injection. Data present by mean ± standard derivation (s.d.), n=3. **(D)** The bioluminescence image of mouse bearing 4T1 xenograft tumor on the right second mammary gland (blue arrow) at 16 hours post intravenous injection of PMPC-nFLuc. **(E)** Quantification of the bioluminescence intensity captured of the region of interest (ROI) positioned on tumor site of mice bearing 4T1 xenograft tumor at different time post intravenous injection of PMPC-nFLuc. Data present by mean ± standard derivation (s.d.),

n=3. **(F)** Quantification of bioluminescence intensity of the main organs (e.g., heart, liver, spleen, lung, kidney and tumor) of the mice bearing 4T1 xenograft tumor at 16 h post intravenous injection of PMPC-nFLuc. Data present by mean ± standard derivation (s.d.), n=3.

3.3 Conclusion

As a conclusion, we have developed a novel bioluminescent probe of extracellular ATP based on FLuc and applied it for tumor diagnosis with high sensitivity and high specificity. The probe achieved via nanocapsule technology improves FLuc stability, reduces the immune clearance, prolongs the circulation time and present a high contrast imaging of the tumor. This method provides an effective and safe route for tumor diagnosis.

3.4 Experimental section

3.4.1 Materials

All chemicals were purchased from Sigma-Aldrich unless otherwise noted and were used as received. Recombinant Escherichia coli (E. coli) expressing Firefly luciferase (FLuc) was purchased from Excellgen Corporateion. The nicel-resin affinity column was purchased from Thermo Scientific. Luciferin potassium salt was purchased from Gold Biotechnology. CellTiter-Blue cell viability assay kit was purchased from Promega Corporation. 4T1, J774A.1 cells were purchased from American Type Culture Collection (ATCC). The Dulbecco's Modified Eagle Medium (DMEM) growth medium, trypsin and Fetal Bovine Serum (FBS) was obtained from Corning. BALB/c mice were purchased from the Jackson Laboratory. The μ-Slide chambered coverslip with 12 wells for fluorescence microscope imaging was purchased from the ibidi.

3.4.2 Instruments

UV-Visible spectra were acquired with a Beckman-Coulter DU730. Dynamic light scattering (DLS) studies of the enzyme nanocomplexes was measured on Zetasizer Nano instrument (Malvern Instruments Ltd., Kingdom). Transmission electron microscope (TEM) images were obtained on T12 Quick CryoEM and CryoET (FEI). The bioluminescence intensity and absorbance were measured with a Tecan Infinite 200 PRO plate reader. Fluorescence-activated cell sorting results were achieved by BD LSRFortessa. The fluorescence microscope images were acquired by Leica dmi8 inverted microscope. The optical imaging and quantification were achieved by IVIS Lumina II (Perkin Elmer).

3.4.3 Production and purification of FLuc

The fusion proteins were expressed in transformed *E. Coli* Rosetta2 and purified using a nicel-resin affinity column (Ni-NTA, Thermo Scientific). Bacteria cells were grown in LB medium at 37°C until reaching 0.8 at OD600. The induction of expression was achieved by adding 1mM isopropyl β-D-thiogalactoside (IPTG) at 16°C for 24h. After induction, *E. coli* cells were harvested by centrifugation and resuspended in purification buffer (200 mM NaCl, 50 mM NaH_2PO_4, pH7.4). The FLuc protein were extracted by sonication.

The purification of FLuc proteins were achieved by Ni-NTA column. Briefly, the protein extracts were passed through a Ni-NTA resin column, which was pre-equilibrated with purification buffer. The weakly bound contaminating proteins were washed off by the purification buffer and the washing buffers (20mM and 40mM imidazole in purification buffer). And the His-tagged FLuc proteins were finally eluted with the elusion buffer (250 mM imidazole

in purification buffer) and dialyzed against PBS buffer to remove imidazole. To maintain the activity of FLuc, all materials were prechilled in 4°C.

3.4.4 Synthesis of the nanocapsules

3.4.4.1 Acryloxylation of the FLuc proteins

The acryloxylation of FLuc enzymes was achieved by conjugating acryloyl groups on cystine residues. Briefly, the reduction of disulfide bonds in FLuc was achieved by incubating the stock solution of FLuc (10 mg/mL in PBS) with 10 mM tris(2-carboxyethyl)phosphine (TCEP) in pH 7.4 at 4 °C for 3 h. Then the stock solution of FLuc was dialyzed against PBS buffer to remove TCEP. And N–(3–aminopropyl) methacrylamide (1% in PBS, *m/v*, APM) was reacted with succinimidyl 4-(N-maleimidomethyl)cyclohexane-1-carboxylate (5% in DMSO, *m/v*, SMCC) with a mole ratio of 1.2:1. Allow the reaction to be incubate at 4 °C overnight until all NHS ester of SMCC reacted. Then, the APM-SMCC solution was added to FLuc stock (10 mg/mL) for acryloxylation with a mole ratio of 10:1. After four-hour incubation at 4 °C, acrylolated FLuc proteins was dialyzed against PBS buffer to remove all unreacted components.

The degree of modification was measured by measuring the cystine residues remained on the FLuc proteins by Ellman's reagent 5,5'-dithio-bis-(2-nitrobenzoic acid) (DTNB). Before the test, the reaction buffer (0.1 M sodium phosphate, pH 8.0, 1mM EDTA0 and Ellman's reagent solution (4 mg/mL DTNB in reaction buffer) were prepared. The standard was then achieved by 2 folds serial dilution of native FLuc and acrylolated FLuc solution (1mg/mL in PBS) in PBS. A set of test tubes, each containing 2 μL of Ellman's reagent solution and 100 μL reaction buffer, were prepared. Added 10 μL of each native or acrylolated FLuc solutions to each test tubes.

Incubated at room temperature for 30 min, the absorbance at 412nm was measured to investigate the average number of acryloyl groups conjugated onto FLuc proteins. As illustrated in Figure 3-5, after 4h reaction, about 5 acryloyl groups were conjugated on to each FLuc proteins. While almost all enzymatic activity of FLuc was remained.

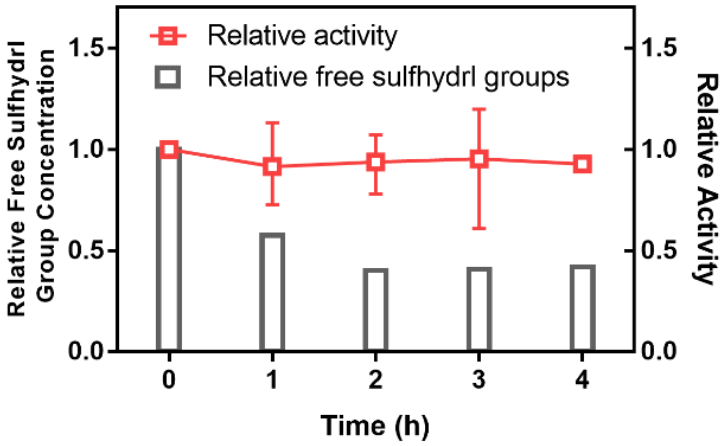

Figure 3-5. Average number of remained thiol groups quantified by Ellman's assay and relative residual activity for 4 hours post reaction.

3.4.4.2 Synthesis of FLuc nanocapsules

After acryloxylation, the FLuc proteins were encapsulated using the *in situ* polymerization method. Reagents for polymerization including 2-methacryloyloxyethyl phosphorylcholine (MPC), acrylamide (AAM) and N-(3-aminopropyl) methacrylamide (APM) were firstly prepared as 40% (m/v), 30% (*m/v*) and 20% (*m/v*) in PBS for stock solution. And N,N'-methylenebisacrylamide (BIS) as the crosslinker was prepared as 10% (*m/v*) in DMSO. To maintain the activity of FLuc, adenosine triphosphate (ATP) and magnesium sulphate ($MgSO_4$)

were prepared as 50 mM in PBS and 100 mM in DI water, respectively. The protein concentration of FLuc was turned to be 35 μM by diluting with PBS buffer. The proteins were then mixed with the monomers (e.g., MPC, AAM, APM) and crosslinkers BIS first with a ratio listed in Table 3-1. Then the polymerization was initiated by adding ammonium persulfate (APS, 10%, *m/v*) and tetramethylethylenediamine (TEMED) and kept at 4 °C for 1 h. After encapsulation, the solution was dialyzed against prechilled PBS buffer to remove unreacted reagents.

Table 3-1 Synthesis parameters of nFLuc nanoparticles

Sample	Protein	MPC	AAM	APM	BIS	APS	TEMED	ATP	$MgSO_4$
PMPC-nFLuc	1	7000	0	0	500	125	2500	100	100
PAAM-nFLuc	1	0	5600	0	500	125	2500	100	100
PAPM-nFLuc	1	0	5200	400	500	125	2500	100	100

The successful encapsulation of FLuc was confirmed by agarose electrophoresis and competed with 1% heparin. As shown in Figure 3-6, the native FLuc (negatively charged) run to the anode direction. While PAPM-nFLuc which was positively charged run to the opposite direction and neutral charged PAAM-nFLuc and PMPC-nFLuc stayed in the well. The protein cores inside were competed with 1% heparin. There was no evidence of FLuc proteins released after competition, confirming the construction of nFLuc nanocapsules.

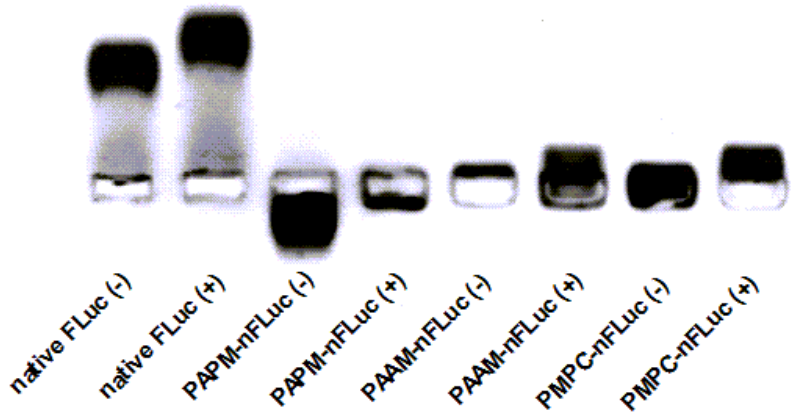

Figure 3-6 Stability of nFLuc nanocapsules against heparin competition for 30 mins via agarose gel electrophoresis.

3.4.4.3 Determination of nFLuc nanocapsule concentration

The concentrations of nFLuc nanoparticles, were determined by Pierce™ BCA Protein Assay Kit. Briefly, native protein FLuc were prepared with a series of enzyme concentrations (1, 0.5, 0.25, 0.125, 0.0625, 0.03125, 0.015625 and 0.0078125 mg/mL). Then, each standard and unknown sample were prepared by mixing 100 μL BCA Reagent A, 2 μL BCA Reagent B and 5 μL sample. Then the mixture was incubated at room temperature for 2 h. Absorbance at 562 nm were measured and compared with the standard curves to calculate the concentration of unknown samples.

3.4.5 TEM and DLS of nanoparticles

TEM samples were prepared as our previous work. Briefly, Drop 2 μL of 0.2 mg/mL nanoparticle solution onto carbon-coated copper grids. After 45s incubation, excess amount of the samples was removed. Then the grid was rinsed with DI water, and stained with 1% sodium phosphotungstate at pH 7.0. To investigate the size and zeta potential of nanoparticles, DLS measurements were taken under the concentration of 0.5 mg/mL. The TEM images of PAPM-nFLuc and PAAM-nFLuc were demonstrated in Figure 3-7. The nFLuc nanocapsules revealed a uniform sphere in the mean diameter of 25 nm. The DLS results illustrated in Figure 3-8 further confirms this result. In addition, the zeta potential of PAAM-nFLuc changed to 0 mV from -9 mV of native FLuc. And the zeta potential of PAPM-nFLuc changed toward 8 mV form -9 mV after encapsulation.

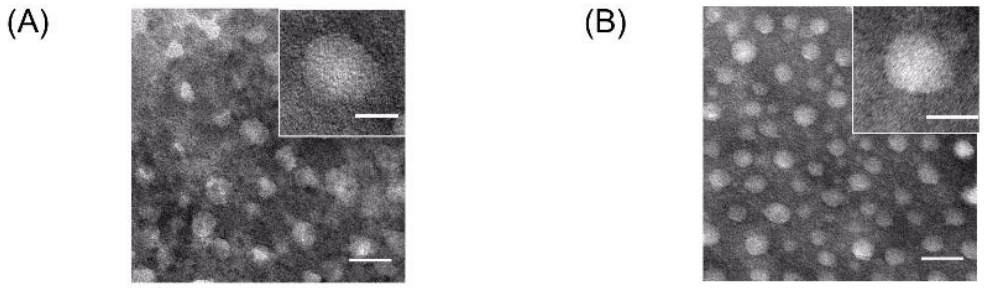

Figure 3-7 TEM images of PAPM-nFLuc (A) and PAAM-nFLuc (B).

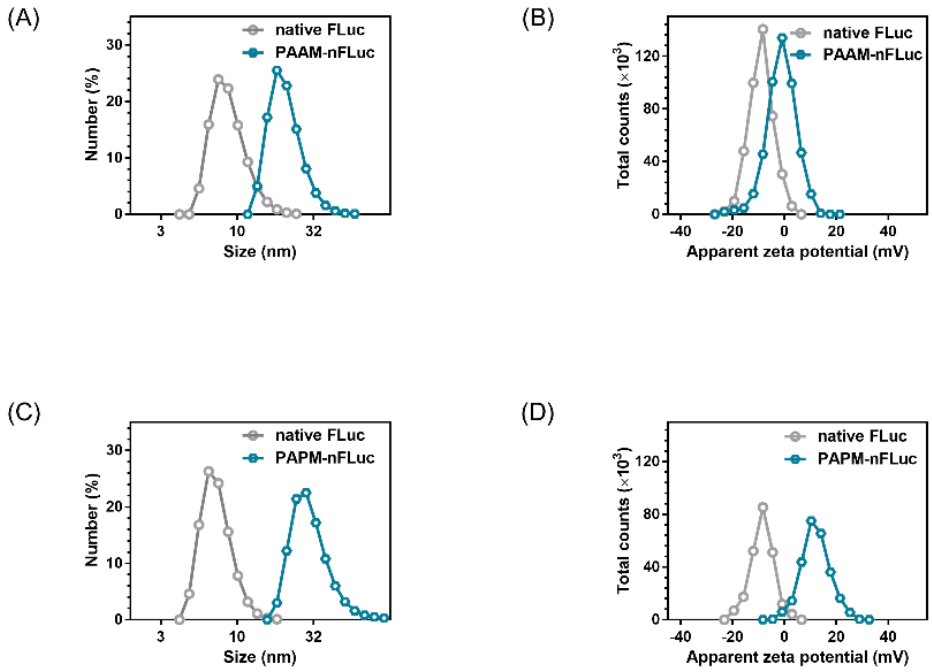

Figure 3-8 The size and zeta potential distribution of PAAM-nFLuc and PAPM-nFLuc. (A) The size distribution of native FLuc and PAAM-nFLuc. **(B)** The zeta potential distribution of native FLuc and PAAM-nFLuc. **(C)** The size distribution of native FLuc and PAPM-nFLuc. **(D)** The zeta potential distribution of native FLuc and PAPM-nFLuc.

3.4.6 Activity assays of nFLuc

The activities of native FLuc and FLuc nanocasules were assessed by monitoring the rate of bioluminescence reaction. Before the activity test, the substrate buffer was prepared with 20mM tricine, 3.74 mM magnesium sulfate, 0.1mM ethylenediaminetetraacetic acid (EDTA) and 2 mM DTT following by adjusting pH to 7.4. The other stock solutions, including Coenzume A (CoA, 10mM in DI water), ATP (50mM in PBS) and Luciferin (10mM in PBS), were prepared. Then, the activity buffer was prepared by mixing 27μL CoA solution, 10.6 μL ATP solution, 47

μL luciferin solution and 915.5 μL substrate buffer solution. For the tests of bioluminescence reaction rate, 2 μL native FLuc or nFLuc solution (2.5 mg/mL) were added to 35 μL activity buffer in a 96-well plate. And the bioluminescence intensity was monitored by the plate reader with an exposure time setting as 1 s.

3.4.7 ATP sensitivity test of nFLuc

To investigate the ATP sensitivity of nFLuc, a series of the activity buffer were prepared with different ATP concentrations. Before the activity test, the substrate buffer was prepared with 20mM tricine, 3.74 mM magnesium sulfate, 0.1mM ethylenediaminetetraacetic acid (EDTA) and 2 mM DTT following by adjusting pH to 7.4. The other stock solutions, including Coenzume A (CoA, 10mM in DI water) and Luciferin (10mM in PBS), were prepared. Then, the activity buffer was prepared by mixing 27μL CoA solution, 47 μL luciferin solution and 915.5 μL substrate buffer solution with 10.6 μL ATP solution of different concentrations. The final concentration of ATP in the activity buffer is 0.05, 0.1, 5, 25, 50, 75, 100 μM. Then the bioluminescence intensity was tested by adding 2 μL native FLuc or nFLuc solution (2.5 mg/mL) to 35 μL activity buffer in a 96-well plate. And the bioluminescence intensity was monitored by the plate reader with an exposure time setting as 1 s.

3.4.8 Cell culture and cell viability test

The mouse mammary gland tumor 4T1 cells and the mouse macrophage J774A.1 cells were purchased from ATCC. The 4T1 and J774A.1 cells were cultured in 25 cm^2 tissue culture flasks (Thermo-Fisher Scientific) with DMEM supplemented with 10% FBS and 1% penicillin/streptomycin. The subculture protocol follows the recommended protocol of ATCC.

Briefly, the 4T1 cells or J774A.1 cells were rinsed by PBS buffer to remove the serum with trypsin inhibitor. Trypsinization was achieved by adding 1 mL trypsin-EDTA solution to the cell culture flask and incubating at 37 °C for about 2 min until the cell detached. When the cell layer was detached, 4 mL DMEM medium with 10% FBS and 1% penicillin/streptomycin was added to stop the trypsinization. The 1 mL the cell suspension was added to the new cell culture flask.

Cell viability of 4T1 cells after incubated with nFLuc were investigated at different concentration. Before viability test, 10^4 cells were seeded into a 96-well plate and cultured in 100 μL DMEM medium with 10% FBS and 1% Pen/Strep for a day. Then PAAM-nFLuc and PAPM-nFLuc were added into each well with concentrations of 200, 400, 600, 800, 1200 nM and incubated with cells for 24 h.

After incubation, CellTilter-Blue (20 μL) was added into each well and further incubated at 37 °C for 3h. Then the fluorescence intensities (Ex=535 nm, Em=585 nm) were quantified with a plate reader. As illustrated in Figure 3-9, the majority of cell viability was retained after incubation with PAAM-nFLuc and PAPM-nFLuc. Therefore, there is no evidence of cytotoxicity of the nFLuc nanocapsules.

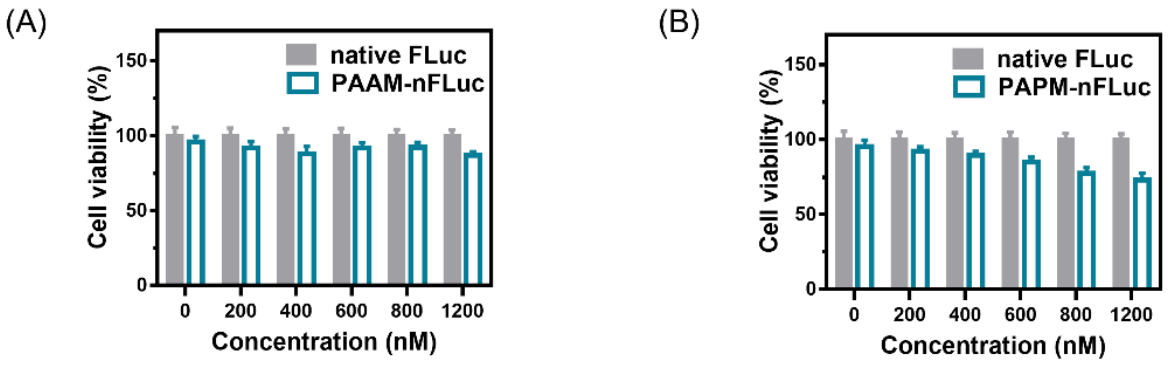

Figure 3-9 Cytotoxicity of PAAM-nFLuc and PAPM-nFLuc. (A) The CellTIter-Blue cell viability assays after incubation with native FLuc and PAAM-nFLuc for 24 hours. **(B)** The CellTiter-Blue cell viability assays after incubation with native FLuc and PAPM-nFLuc for 24 hours.

3.4.9 Stability assays of FLuc and nFLuc

3.4.9.1 Stability test against high temperature

The stability assays of native FLuc and nFLuc were tested by monitoring the activity of enzymes incubated with PBS at 37 °C. The FLuc samples (2.5 mg/mL) were directly diluted in PBS with the volume ratio of 1:10. Samples were then incubated in 37 °C. And the activity of FLuc was tested at different incubation time. The stability of PAAM-nFLuc and PAPM-nFLuc were compared with the native FLuc in 37 °C. As demonstrated in Figure 3-10, the native FLuc lost more than 90% of the activity after 40 min incubation. While for the nFLuc nanocapsules, more than 80% of the activity maintained. Thus, the stability of PAAM-nFLuc and PAPM-nFLuc was significantly increased compared with the native FLuc, allowing it to be applied as a probe molecule in vivo.

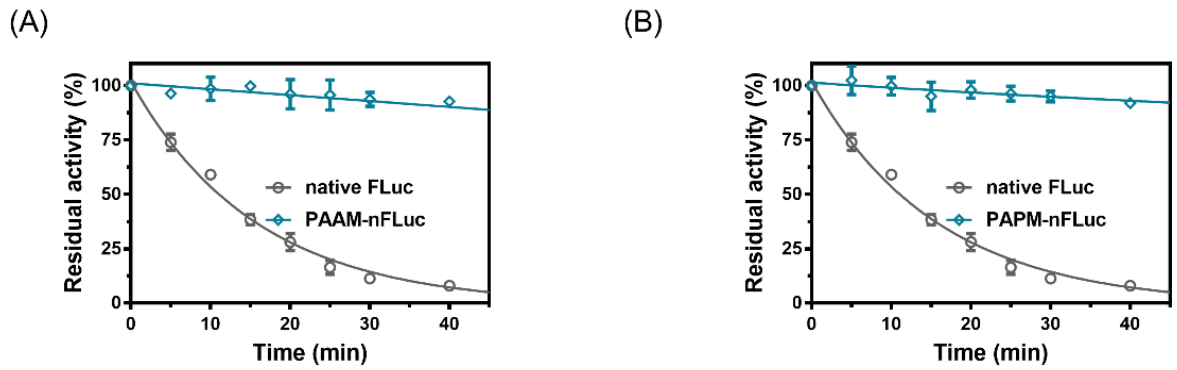

Figure 3-10 Thermal stability of native FLuc and nFLuc nanocapsules. (A) Relative residual activity of native FLuc and PAAM-nFLuc after incubation at 37 °C. **(B)** Relative residual activity of native FLuc and PAPM-nFLuc after incubation at 37 °C.

3.4.9.2 Stability test against protease degradation

The stability assays of native FLuc and nFLuc against protease were tested by monitoring the activity of enzymes incubated with trypsin at 37 °C. Briefly, the FLuc samples (2.5 mg/mL) were directly diluted in 0.11 mg/mL trypsin in PBS buffer with the volume ratio of 1:10, making the final concentration of trypsin 0.1mg/mL. Samples were then incubated in 37 °C. And the activity of FLuc was tested at different incubation time. The stability of PAAM-nFLuc and PAPM-nFLuc were compared with the native FLuc in 37 °C. As demonstrated in Figure 3-11, the native FLuc lost almost all of the activity after 20 min incubation. While for the nFLuc nanocapsules, more than 70% of the activity maintained. Thus, the stability of PAAM-nFLuc and PAPM-nFLuc against protease was significantly increased compared with the native FLuc, allowing it to be applied as a probe molecule in vivo.

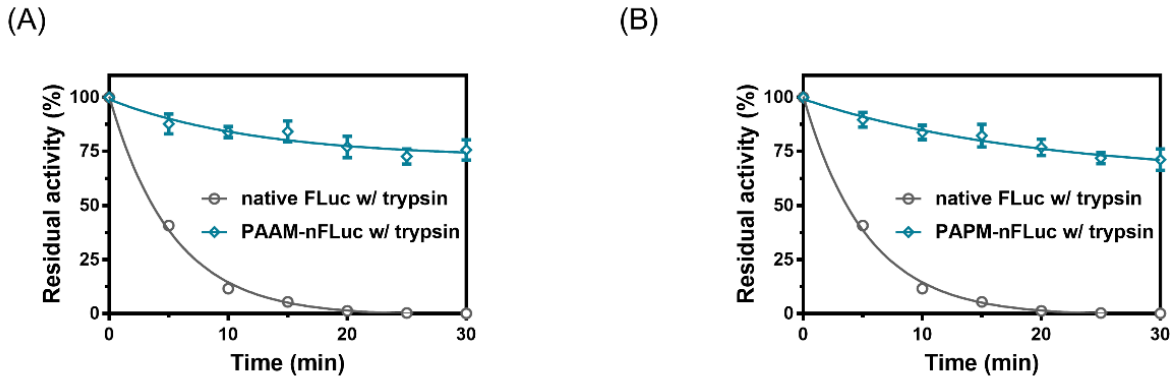

Figure 3-11 Stability PAAM-nFLuc and PAPM-nFLuc against protease degradation. (A) Relative residual activity of native FLuc and PAAM-nFLuc with 0.1 mg/mL trypsin after incubation at 37 °C. **(B)** Relative residual activity of native FLuc and PAPM-nFLuc with 0.1 mg/mL trypsin after incubation at 37 °C.

3.4.9.3 Stability test in mouse serum

To investigate the stability of native FLuc and all nFLuc nanocapsules in the blood, the samples (1 mg/mL) were diluted in mouse serum (50 mg/mL) with a volume ratio of 1:10. Then the mixtures were incubated at 37 °C for 4 hours. In addition, Mouse serum incubated with PBS buffer was used as control. After incubation, the mixture was diluted with DI water with a volume ration of 1:100 and the size distribution of the mixture was evaluated by DLS.

3.4.9.4 Stability test in vivo

The stability of PMPC-nFLuc in vivo was evaluated by subcutaneous injection of the nFluc nanocapsules. Briefly, the PMPC-nFLuc 4 mg/mL in PBS was filtered by 0.22 μM filter. The 5-week old BALB/c mice were administrated 50 μL filtered PMPC-nFLuc solutions subcutaneously. The native FLuc solution in 4 mg/mL was filtered and administrated in the same mouse as control. For bioluminescence imaging, luciferin (125 mg/kg body weight) was intraperitoneally injected using a 28-30 G needle prior to imaging. Then the mice were transferred into a plexiglass imaging chamber, which allows continued administration of oxygen and isoflurane and is warmed to keep the body temperature of animal stable. Bioluminescence imaging was performed by IVIS Lumina II (Perkin Elmer) without interrupting the anesthesia at

15 min, 24 h, 36 h, 48 h, 60 h and 72 h post injection. Then the luminescence intensity in the region of interest was quantified by IVIS Lumina software.

3.4.10 Fluorescence imaging and fluorescence-activated cell sorting (FACS) test

The cell internalization kinetics were assessed via the fluorescence microscope and fluorescence activated cell sorting (FACS). 4T1 cells were cultured in DMEM medium with 10%FBS and 1% penicillin/streptomycin. After 2 days incubation, cells reached 10^4 cells in each well the μ-Slide chambered coverslip with 12 wells. Nanocapsules labelled with rhodamine B were pre-incubated with mouse serum (50 mg/mL) in 37 °C for 3 hours allowing the samples to be opsonized. And then the nFLuc nanocapsules (0.4 mg/mL) with and without mouse serum incubation were incubated with the J774A.1 cells for 2 h incubation. The native FLuc labelled with rhodamine B was used as control.

For fluorescence microscopy test, the cells were rinsed with PBS for three times and fixed with 4% paraformaldehyde for 15 min at room temperature. Then cells were rinsed with PBS and visualized with a fluorescent microscope. For FACS analysis, cells were rinsed with PBS, fixed with paraformaldehyde, trypsinized, centrifuged and re-suspended in PBS and then analyzed with flow cytometry. As illustrated in Figure 3-12, J774A.1 cells incubated with the positively charged PAPM-nFLuc nanocapsules showed strong fluorescence intensity. And with the pre-incubation with mouse serum, the fluorescence signal further increased, suggesting a high level of phagocytosis for PAPM-nFLuc nanocapsules. While the native FLuc and PAAM-nFLuc showed a little fluorescent when incubated with J774A.1 cells without pre-incubation with mouse serum. But after incubated with mouse serum, the J774A.1 cells were fluorescent,

suggesting that serum pre-incubation opsonized the native FLuc and PAAM-nFLuc and enhanced their phagocytosis. However, the macrophages incubated with PMPC-nFLuc nanocapsules, on the other hand, exhibited almost no phagocytosis with or without mouse serum. The FACS analysis was consistent with the fluorescence microscopy methods.

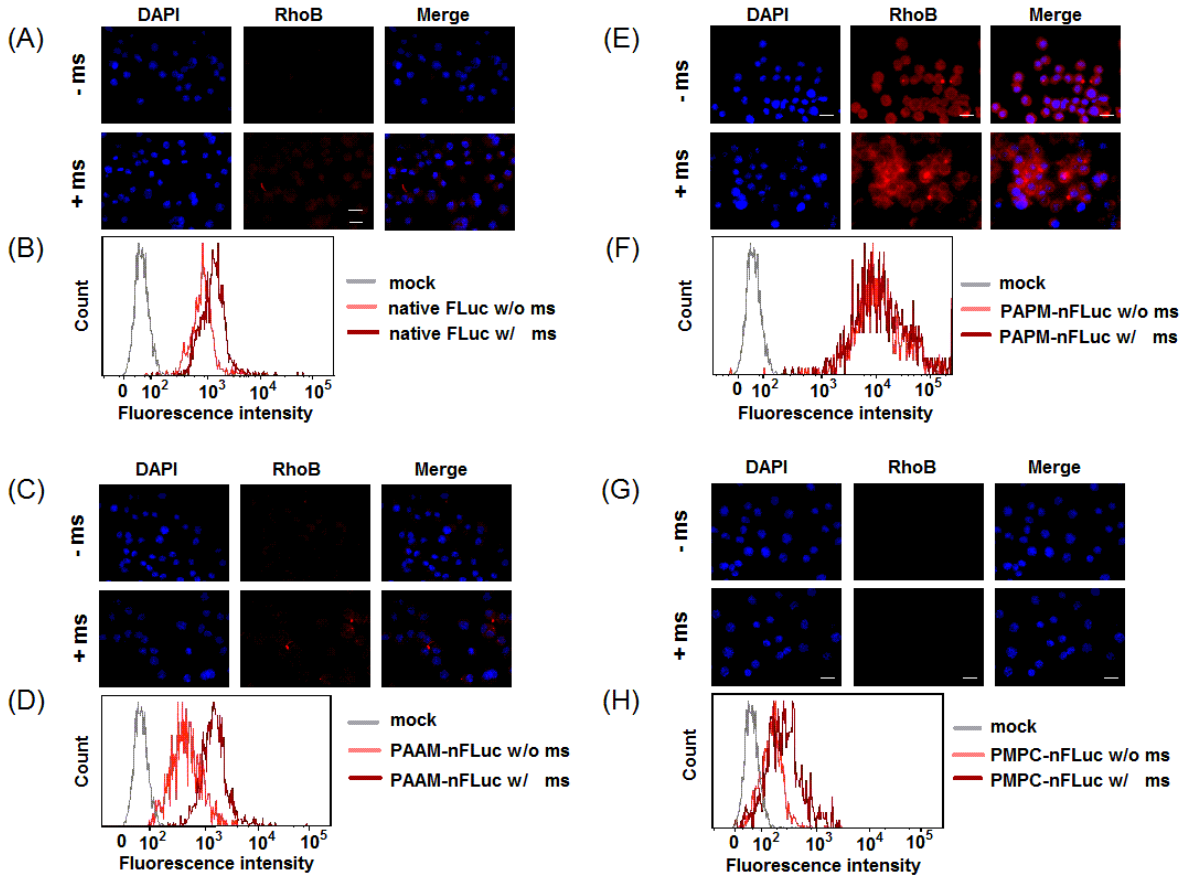

Figure 3-12. Phagocytosis of nFLucs. (A), (C), (E), (G) Fluorescence images to compare J774A.1 mouse macrophage uptake of native FLuc, PAAM-nFLuc, PAPM-nFLuc and PMPC-nFLuc with (+ ms) and without mouse serum (- ms) respectively. **(B), (D), (F), (H)** Fluorescence-assisted cell sorting (FACS) analysis of J774A.1 mouse macrophages at 3 hours post incubation with native FLuc, PAAM-nFLuc, PAPM-nFLuc and PMPC-nFLuc in 37 °C.

3.4.11 Protein adsorption test

The protein adsorption assay was tested by incubated 1 mg/mL native FLuc, PMPC-nFLuc, PAAM-nFLuc and PAPM-nFLuc with the whole mice serum at a volume ratio of 1:1 in 37 ℃ for 1 h. The samples were filtered with centricon (molecular weight cut-off, MWCO=300kDa) and washed by PBS buffer for 3 times to remove unabsorbed proteins. Both adsorbed and flow-through samples were collected and measured by BCA assay. The total amount with adsorbed and flow-through samples were calculated as 100 %.

3.4.12 Pharmacokinetics analysis of PMPC-nFLuc nanocapsules via intravenous injection

The pharmacokinetics of PMPC-nFLuc and native FLuc in mouse plasma were achieved by monitoring the activity of Fluc in the plasma. Briefly, male BALB/c mice of 5-week-old were purchased from the Jackson Laboratory. The mice were administrated 100 μL PMPC-nFLuc (4 mg/mL) via tail vein injection. The native FLuc in the same concentration were injected as control. The blood samples (20 μL) were collected from the tail vein of the mice at 1 h, 4 h, 8 h, 16 h, 24 h, 36 h and 48 h post injection. After collection, the blood samples were immediately centrifuged at 5000 rpm for 2 min to remove the blood cells. The supernatant was centrifuged again at 5000 rpm for 2 min to make sure the blood cells were completely removed. The supernatant was collected as the mouse plasma samples. Then the activity of nFLuc and native FLuc were monitored with the protocol previously described by a Tecan Infinite 200 PRO plate reader.

3.4.13 Construction of tumor model

The formulation of 4T1 tumor was conducted as described in the literature. In brief, the 4T1 cells were cultured in 25 cm^2 tissue culture flasks (Thermo-Fisher Scientific) with DMEM supplemented with 10% FBS and 1% penicillin/streptomycin for 2 days. Then the 4T1 cells were rinsed by PBS buffer to remove the serum with trypsin inhibitor. Trypsinization was achieved by adding 1 mL trypsin-EDTA solution to the cell culture flask and incubating at 37 °C for about 2 min until the cell detached. The detached cells were mixed with DMEM supplemented with 10% FBS, centrifuged and re-suspended in PBS to remove all medium and trypsin solution. Then 5×10^5 4T1 cells were counted by hemocytometer and suspended in 50 μL PBS. The cells were subcutaneously injected into the second mammary gland of female Balb/C mice to construct syngenic orthotopic tumor. The size of the tumor was measured everyday by vernier caliper.

3.4.14 Bioluminescence imaging

After injection of 4T1 cells, the size of the tumor was monitored every day. Until the size of the tumor reached 5 mm in diameter, the mice were used by bioluminescence imaging. The PMPC-nFLuc samples (100 μL) were diluted in PBS buffer for 4 mg/mL and intravenously injected to the mice via tail vein. Then the luciferin (125 mg/kg body weight) was intraperitoneally injected using a 28-30 G needle prior to imaging. Then the mice were transferred into a plexiglass imaging chamber, which allows continued administration of oxygen and isoflurane and is warmed to keep the body temperature of animal stable. Bioluminescence imaging was performed by IVIS Lumina II (Perkin Elmer) without interrupting the anesthesia at 1, 16, 24 and 48 h post injection. Then the luminescence intensity in the tumor site was quantified by IVIS Lumina software.

3.4.15 Biodistribution of PMPC-nFLuc nanocapsules

The biodistribution of nanocapsules were investigated by optical imaging. The 5-week-old BALB/c mice were purchased from the Jackson Laboratories and constructed with 4T1 tumor model. Until the size of the tumor reached 5 mm in diameter, the mice were used by bioluminescence imaging. The PMPC-nFLuc samples (100 μL) were diluted in PBS buffer for 4 mg/mL and intravenously injected to the mice via tail vein. Then the luciferin (125 mg/kg body weight) was intraperitoneally injected using a 28-30 G needle at 30 min prior to imaging. Post 16 h of injection, PBS buffer were perfused through the vascular system to achieve a whole animal blood removal. Worth noting that, the time and pressure of perfuse need to be quick and low to avoid perfuse all luciferin substrates diffused in the organs. Then the main organs, including the heart, liver, spleen, lung, kidney and tumor were harvested for ex vivo optical imaging. The luminescence intensity of organs was then observed and quantified by IVIS Lumina II (Perkin Elmer).

Chapter 4. Conclusion

Protein delivery has been considered as a safe, direct, highly sensitive and highly specific approach for therapeutic and diagnostic purposes. However, the efficient responses of protein therapeutics are limited since the biological barriers prevent them to successfully accumulation at targeting sites. Extensive efforts have been made in recent decades to develop strategies and carriers for efficient protein delivery, such as liposome, polymeric nanoparticles, cationic coating, CPP or targeting agent conjugation and etc. However, many of these approaches fail to address such biological barriers. New strategies need to be develop for overcoming these barriers. In addition, the behavior of protein delivery process need to be fully understand for a rational design for novel protein delivery platforms.

Our group developed a novel platform of protein delivery by encapsulating a single protein molecule with a thin layer of polymer network, named as protein nanocapsules. The synthesis process of the protein nanocapsules involves two steps. The protein cores are first conjugated or adsorbed with polymerizable vinyl groups on the surface. Then in situ polymerization can be initiated to achieve a thin layer of polymer wrapping the protein molecules. This system endows new features and surface properties to a large library of proteins.

My Ph.D. research focuses on develop various protein nanocapsules based on our in situ polymerization system to overcome three different level of biological barriers, the cell membrane barrier, the MPS barrier and the BBB. And applied to these protein nanocapsules in real-time monitoring the internalization kinetics of current nanocarriers, cancer diagnosis, and efficient CNS delivery.

In cellular level, I develop a FLuc nanocapsules, which can mimic current strategies for intracellular delivery, as a probe to real-time quantify the internalization process. By realizing

precisely spatiotemporal control over distribution and functions, this platform provides a simple and efficient approach for optimization of dosimetry, characterization of therapeutic efficiency and screening of novel medicine. It can be extended to evaluate the internalization kinetics profiles of other nanostructure-based delivery systems.

In systematic level, I synthesized another FLuc nanocapsules with stealth surface. The probe improves FLuc stability, reduces the immune clearance, prolongs the circulation time and present a high contrast imaging of the tumor. This method provides an effective and safe route for tumor diagnosis.

As a summary, my research establishes novel strategies to understand, design, synthesize and apply nanocarriers for protein delivery to achieve an efficient delivery across various biological barriers.

Reference

1. Leader, B., Baca, Q. J. & Golan, D. E. Protein therapeutics: a summary and pharmacological classification. *Nat. Rev. Drug Discov.* **7,** 21–39 (2008).
2. Pennisi, E. Gene counters struggle to get the right answer. *search.proquest.com*
3. International Human Genome Sequencing Consortium. Initial sequencing and analysis of the human genome. *nature.com*
4. Venter, J. C., Adams, M. D., Myers, E. W. & Li -, P. W. The sequence of the human genome. *science.sciencemag.org*
5. Banting, F. G., Best, C. H. & Collip, J. B. Pancreatic extracts in the treatment of diabetes mellitus. *ncbi.nlm.nih.gov*
6. Jones, R. H., Maccuish, A. C., Watkins, P. J. & Glynne, A. Biosynthetic human insulin in the treatment of diabetes: a double-blind crossover trial in established diabetic patients. *Elsevier*
7. Finkelstein, B. S., Imperiale, T. F. & Speroff, T. Effect of growth hormone therapy on height in children with idiopathic short stature: a meta-analysis. *jamanetwork.com*
8. Hokken-Koelega, A. C. S. & de Munck Keizer-Schrama, S. Growth hormone treatment in growth-retarded adolescents after renal transplant. *Elsevier*
9. Osborne, S., Reynolds, S., George, N. & Lindemayer -, F. Challenging endoscopy reprocessing guidelines: a prospective study investigating the safe shelf life of flexible endoscopes in a tertiary gastroenterology unit. *researchgate.net*
10. Benz, R. L., Pressman, M. R. & Hovick, E. T. A preliminary study of the effects of correction of anemia with recombinant human erythropoietin therapy on sleep, sleep disorders, and daytime sleepiness in …. *ajkd.org*

11. Miles, S. The use of hematopoietic growth factors in treating HIV infection. *europepmc.org*

12. Lieschke, G. J. & Burgess, A. W. Granulocyte colony-stimulating factor and granulocyte-macrophage colony-stimulating factor. *Mass Medical Soc*

13. Corwin, H. L., Gettinger, A., Pearl, R. G., Fink, M. P. & Levy, M. M. Efficacy of recombinant human erythropoietin in critically ill patients: a randomized controlled trial. *jamanetwork.com*

14. Boxer, A. M., Gottesman, N. & Bernstein, H. Debridement of dermal ulcers and decubiti with collagenase. *europepmc.org*

15. Rao, D. B., Sane, P. G. & Georgiev, E. L. Collagenase in the treatment of dermal and decubitus ulcers. *Wiley Online Library*

16. Clavell, L. A., Gelber, R. D. & Cohen, H. J. Four-agent induction and intensive asparaginase therapy for treatment of childhood acute lymphoblastic leukemia. *Mass Medical Soc*

17. Greinacher, A., Völpel, H. & Janssens, U. Recombinant hirudin (lepirudin) provides safe and effective anticoagulation in patients with heparin-induced thrombocytopenia: a prospective study. *Am Heart Assoc*

18. Hurwitz, H., Fehrenbacher, L. & Novotny, W. Bevacizumab plus irinotecan, fluorouracil, and leucovorin for metastatic colorectal cancer. *Mass Medical Soc*

19. Ferrara, N., Hillan, K. J. & Gerber, H. P. Discovery and development of bevacizumab, an anti-VEGF antibody for treating cancer. *nature.com*

20. Keating, M. J., O'Brien, S. & Albitar, M. Early results of a chemoimmunotherapy regimen of fludarabine, cyclophosphamide, and rituximab as initial therapy for chronic lymphocytic leukemia. *pdfs.semanticscholar.org*

21. Gaetano, N. D., Xiao, Y., Erba, E. & Bassan, R. Synergism between fludarabine and rituximab revealed in a follicular lymphoma cell line resistant to the cytotoxic activity of either drug alone. *Wiley Online Library*

22. Jazirehi, A. R., Huerta-Yepez, S., Cheng, G. & Bonavida, B. Rituximab (chimeric anti-CD20 monoclonal antibody) inhibits the constitutive nuclear factor-κB signaling pathway in non-Hodgkin's lymphoma B-cell lines: role in …. *AACR*

23. Vogel, C. L., Cobleigh, M. A. & Tripathy, D. Efficacy and Safety of Trastuzumab as a Single Agent in First-Line Treatment of HER2-Overexpressing Metastatic Breast Cancer. *quantason.com*

24. Genovese, M. C., Becker, J. C. & Schiff, M. Abatacept for rheumatoid arthritis refractory to tumor necrosis factor α inhibition. *Mass Medical Soc*

25. Cohen, S., Hurd, E., Cush, J. & Schiff, M. ⋯ of rheumatoid arthritis with anakinra, a recombinant human interleukin‐1 receptor antagonist, in combination with methotrexate: Results of a twenty‐four–week ⋯. *Wiley Online Library*

26. Denton, M. D., Magee, C. C. & Sayegh, M. H. Immunosuppressive strategies in transplantation. *thelancet.com*

27. Nashan, B., Moore, R., Amlot, P. & Schmidt, A. G. Randomised trial of basiliximab versus placebo for control of acute cellular rejection in renal allograft recipients. *Elsevier*

28. Abramowicz, D. Daclizumab to prevent acute rejection in renal transplantation. *repository.uantwerpen.be*

29. Szmuness, W., Stevens, C. E. & Harley, E. J. Hepatitis B vaccine: demonstration of efficacy in a controlled clinical trial in a high-risk population in the United States. *Mass Medical Soc*

30. Crosnier, J., Jungers, P., Couroucé, A. M. & Laplanche, A. Randomised placebo-controlled trial of hepatitis B surface antigen vaccine in French haemodialysis units: II, haemodialysis patients. *Elsevier*

31. MacKenzie, I. Z., Bichler, J., Mason, G. C. & Lunan, C. B. Efficacy and safety of a new, chromatographically purified rhesus (D) immunoglobulin. *ejog.org*

32. Ghigo, E., Aimaretti, G., Gianotti, L., Bellone, J. & Arvat, E. New approach to the diagnosis of growth hormone deficiency in adults. *EFES*

33. Mason, H. S., Warzecha, H., Mor, T. & Arntzen, C. J. Edible plant vaccines: applications for prophylactic and therapeutic molecular medicine. *Elsevier*

34. Wurm, F. & Bernard, A. Large-scale transient expression in mammalian cells for recombinant protein production. *Elsevier*

35. Zoller, M. J. New molecular biology methods for protein engineering. *Elsevier*

36. Brannigan, J. A. & Wilkinson, A. J. Protein engineering 20 years on. *nature.com*

37. Mahmood, I. & Green, M. D. Pharmacokinetic and pharmacodynamic considerations in the development of therapeutic proteins. *Springer*

38. Schellekens, H. Bioequivalence and the immunogenicity of biopharmaceuticals. *nature.com*

39. Conner, S. D. & Schmid, S. L. Regulated portals of entry into the cell. *Nature* **422,** 37–44 (2003).

40. Aderem, A. & Underhill, D. M. Mechanisms of phagocytosis in macrophages. *annualreviews.org*

41. Hall, A. & Nobes, C. D. Rho GTPases: molecular switches that control the organization and dynamics of the actin cytoskeleton. *rstb.royalsocietypublishing.org*

42. Chimini, G. & Chavrier, P. Function of Rho family proteins in actin dynamics during phagocytosis and engulfment. *nature.com*

43. Ridley, A. J. Rho proteins: linking signaling with membrane trafficking. *Wiley Online Library*

44. Anderson, R. G. The caveolae membrane system. *Annu. Rev. Biochem.* **67,** 199–225 (1998).

45. Drab, M., Verkade, P., Elger, M., Kasper, M. & Lohn -, M. Loss of caveolae, vascular dysfunction, and pulmonary defects in caveolin-1 gene-disrupted mice. *science.sciencemag.org*

46. Edidin, M. Shrinking patches and slippery rafts: scales of domains in the plasma membrane. *Elsevier*

47. Damke, H., Baba, T. & van der Bliek, A. M. Clathrin-independent pinocytosis is induced in cells overexpressing a temperature-sensitive mutant of dynamin. *jcb.rupress.org*

48. Frank, M. M. & Fries, L. F. The role of complement in inflammation and phagocytosis. *Elsevier*

49. Sarma, J. V. & Ward, P. A. The complement system. *Springer*

50. Singer, L., Colten, H. R. & Wetsel, R. A. Complement C3 deficiency: human, animal, and experimental models. *karger.com*

51. Douchkov, D., Baum, T., Ihlow, A. & Schweizer, P. Microphenomics for interactions of barley with fungal pathogens. *Springer*

52. Friedemann, U. Blood-brain barrier. *Am Physiological Soc*

53. Abbott, N. J., Rönnbäck, L. & Hansson, E. Astrocyte–endothelial interactions at the blood–brain barrier. *nature.com*

54. Pardridge, W. M. The blood-brain barrier: bottleneck in brain drug development. *Elsevier*

55. Hawkins, B. T. & Egleton, R. D. Pathophysiology of the blood–brain barrier: animal models and methods. *Elsevier*

56. Hawkins, B. T. & Davis, T. P. The blood-brain barrier/neurovascular unit in health and disease. *ASPET*

57. Cardoso, F. L., Brites, D. & Brito, M. A. Looking at the blood–brain barrier: molecular anatomy and possible investigation approaches. *Elsevier*

58. Stewart, P. A. Endothelial vesicles in the blood–brain barrier: are they related to permeability? *Springer*

59. Rip, J., Schenk, G. J. & De Boer, A. G. Differential receptor-mediated drug targeting to the diseased brain. *Taylor & Francis*

60. Hervé, F., Ghinea, N. & Scherrmann, J. M. CNS delivery via adsorptive transcytosis. *Springer*

61. Pardridge, W. M. Drug and gene targeting to the brain via blood–brain barrier receptor-mediated transport systems. *Elsevier*

62. Jain, S., Mishra, V., Singh, P., Dubey, P. K. & Saraf, D. K. RGD-anchored magnetic liposomes for monocytes/neutrophils-mediated brain targeting. *Elsevier*

63. Chrétien, F., Lortholary, O. & Kansau, I. Pathogenesis of Cerebral Cryptococcus neoformans Infection after Fungemia. *academic.oup.com*

64. Malam, Y., Loizidou, M. & Seifalian, A. M. Liposomes and nanoparticles: nanosized vehicles for drug delivery in cancer. *Elsevier*

65. Hajos, F., Stark, B., Hensler, S. & Prassl, R. Inhalable liposomal formulation for vasoactive intestinal peptide. *Elsevier*

66. Chou, L. Y. T., Ming, K. & Chan, W. C. W. Strategies for the intracellular delivery of nanoparticles. *pubs.rsc.org*

67. Leroueil, P. R., Hong, S. & Mecke, A. Nanoparticle interaction with biological membranes: does nanotechnology present a Janus face? *ACS Publications*

68. Herrero, M. A., Toma, F. M. & Al-Jamal, K. T. Synthesis and characterization of a carbon nanotube− dendron series for efficient siRNA delivery. *ACS Publications*

69. Chatterjee, D. K., Rufaihah, A. J. & Zhang, Y. Upconversion fluorescence imaging of cells and small animals using lanthanide doped nanocrystals. *Elsevier*

70. Torchilin, V. P. & Rammohan, R. TAT peptide on the surface of liposomes affords their efficient intracellular delivery even at low temperature and in the presence of metabolic inhibitors. *National Acad Sciences*

71. Torchilin, V. P. Tat peptide-mediated intracellular delivery of pharmaceutical nanocarriers. *Elsevier*

72. Derossi, D., Chassaing, G. & Prochiantz, A. Trojan peptides: the penetratin system for intracellular delivery. *Elsevier*

73. Gupta, B., Levchenko, T. S. & Torchilin, V. P. Intracellular delivery of large molecules and small particles by cell-penetrating proteins and peptides. *Elsevier*

74. Torchilin, V. P. Recent approaches to intracellular delivery of drugs and DNA and organelle targeting. *annualreviews.org*

75. Bareford, L. M. & Swaan, P. W. Endocytic mechanisms for targeted drug delivery. *Elsevier*

76. Rajendran, L., Knölker, H. J. & Simons, K. Subcellular targeting strategies for drug design and delivery. *nature.com*

77. Pisal, D. S. & Kosloski, M. P. Delivery of therapeutic proteins. *Wiley Online Library*

78. Tirelli, N., Lutolf, M. P., Napoli, A. & Hubbell, J. A. Poly (ethylene glycol) block copolymers. *Elsevier*

79. Potschka, H. Role of CNS efflux drug transporters in antiepileptic drug delivery: overcoming CNS efflux drug transport. *Elsevier*

80. Wong, H. L., Wu, X. Y. & Bendayan, R. Nanotechnological advances for the delivery of CNS therapeutics. *Elsevier*

81. Misra, A., Ganesh, S., Shahiwala, A. & Shah, S. P. Drug delivery to the central nervous system: a review. *sites.ualberta.ca*

82. Kreuter, J. Drug delivery to the central nervous system by polymeric nanoparticles: what do we know? *Elsevier*

83. Tosi, G., Costantino, L., Ruozi, B. & Forni, F. Polymeric nanoparticles for the drug delivery to the central nervous system. *Taylor & Francis*

84. Singh, R. & Jr, J. L. Nanoparticle-based targeted drug delivery. *Elsevier*

85. Yan, M. *et al.* A novel intracellular protein delivery platform based on single-protein nanocapsules. *nature.com*

86. Gu, Z. *et al.* Protein nanocapsule weaved with enzymatically degradable polymeric network. *ACS Publications*

87. Du, J., Yan, M., Wang, J., Shen, M. & Lu, Y. Controlled Protein Delivery Based on Enzyme-Responsive Nanocapsules. *Wiley Online Library*

88. Zhu, S., Nih, L., Carmichael, S. T. & Lu, Y. Enzyme-Responsive Delivery of Multiple Proteins with Spatiotemporal Control. *Wiley Online Library*

89. Daubs, M. D., Yang, X., Yuan, X., Wang, J. C. & Lu, Y. Growth-factor nanocapsules that enable tunable controlled release for bone regeneration. *ACS Publications*

90. Chen, I. S. Y. *et al.* Phosphorylcholine polymer nanocapsules prolong the circulation time and reduce the immunogenicity of therapeutic proteins. *Springer*

91. Stewart, M. P. *et al.* In vitro and ex vivo strategies for intracellular delivery. *Nature* **538,** 183–192 (2016).

92. Torchilin, V. Intracellular delivery of protein and peptide therapeutics. *Drug Discov. Today. Technol.* **5,** e95–e103 (2008).

93. Verma, A. & Stellacci, F. Effect of surface properties on nanoparticle-cell interactions. *Small* **6,** 12–21 (2010).

94. Gratton, S. E. A. *et al.* The effect of particle design on cellular internalization pathways. *Proc. Natl. Acad. Sci. USA* **105,** 11613–11618 (2008).

95. Papapetrou, E. P. *et al.* Stoichiometric and temporal requirements of Oct4, Sox2, Klf4, and c-Myc expression for efficient human iPSC induction and differentiation. *Proc. Natl. Acad. Sci. USA* **106,** 12759–12764 (2009).

96. Kamiya, H., Akita, H. & Harashima, H. Pharmacokinetic and pharmacodynamic considerations in gene therapy. *Drug Discov. Today* **8,** 990–996 (2003).

97. Teeguarden, J. G., Hinderliter, P. M., Orr, G., Thrall, B. D. & Pounds, J. G. Particokinetics in vitro: dosimetry considerations for in vitro nanoparticle toxicity assessments. *Toxicol. Sci.* **95,** 300–312 (2007).

98. Ferrari, R. *et al.* Investigation of size, surface charge, PEGylation degree and concentration on the cellular uptake of polymer nanoparticles. *Colloids Surf. B Biointerfaces* **123,** 639–647 (2014).

99. He, C., Hu, Y., Yin, L., Tang, C. & Yin, C. Effects of particle size and surface charge on cellular uptake and biodistribution of polymeric nanoparticles. *Biomaterials* **31,** 3657–3666 (2010).

100. Farkhani, S. M. *et al.* Cell penetrating peptides: efficient vectors for delivery of nanoparticles, nanocarriers, therapeutic and diagnostic molecules. *Peptides* **57,** 78–94 (2014).

101. Sanders, W. S., Johnston, C. I., Bridges, S. M., Burgess, S. C. & Willeford, K. O. Prediction of cell penetrating peptides by support vector machines. *PLoS Comput. Biol.* **7,** e1002101 (2011).

102. Milletti, F. Cell-penetrating peptides: classes, origin, and current landscape. *Drug Discov. Today* **17,** 850–860 (2012).

103. RGDpeptidesinduceapoptosis bydirect caspase-3 activation.

104. Danhier, F., Le Breton, A. & Préat, V. RGD-based strategies to target alpha(v) beta(3) integrin in cancer therapy and diagnosis. *Mol. Pharm.* **9,** 2961–2973 (2012).

105. Mishra, S., Webster, P. & Davis, M. E. PEGylation significantly affects cellular uptake and intracellular trafficking of non-viral gene delivery particles. *Eur. J. Cell Biol.* **83,** 97–111 (2004).

106. Lippincott-Schwartz, J. & Patterson, G. H. Development and use of fluorescent protein markers in living cells. *Science (80-.).* **300,** 87–91 (2003).

107. Gregersen, K. A. D. *et al.* Intracellular delivery of bioactive molecules using light-addressable nanocapsules. *ACS Nano* **4,** 7603–7611 (2010).

108. Stephens, D. J. & Allan, V. J. Light microscopy techniques for live cell imaging. *Science (80-.).* **300,** 82–86 (2003).

109. Watson, P., Jones, A. T. & Stephens, D. J. Intracellular trafficking pathways and drug delivery: fluorescence imaging of living and fixed cells. *Adv. Drug Deliv. Rev.* **57,** 43–61 (2005).

110. Chithrani, B. D., Ghazani, A. A. & Chan, W. C. W. Determining the size and shape dependence of gold nanoparticle uptake into mammalian cells. *Nano Lett* **6,** 662–668 (2006).

111. Cho, E. C., Xie, J., Wurm, P. A. & Xia, Y. Understanding the role of surface charges in cellular adsorption versus internalization by selectively removing gold nanoparticles on the cell surface with a I2/KI etchant. *Nano Lett* **9,** 1080–1084 (2009).

112. DELUCA, M., WANNLUND, J. O. N. & MCELROY. Factors Affecting the Kinetics of Light Emission from Crude and Purified Firefly Luciferasel.

113. Ignowski, J. M. & Schaffer, D. V. Kinetic analysis and modeling of firefly luciferase as a quantitative reporter gene in live mammalian cells. *Biotechnol. Bioeng.* **86,** 827–834 (2004).

114. Mo, R., Jiang, T., Sun, W. & Gu, Z. ATP-responsive DNA-graphene hybrid nanoaggregates for anticancer drug delivery. *Biomaterials* **50,** 67–74 (2015).

115. Morciano, G. *et al.* Use of luciferase probes to measure ATP in living cells and animals. *Nat. Protoc.* **12,** 1542–1562 (2017).

116. Tarver, T. Cancer Facts & Figures 2012. American Cancer Society (ACS)' ' Atlanta, GA: American Cancer Society, 2012. 66 p., pdf. Available from. (2012).

117. Siegel, R. L., Miller, K. D. & Jemal, A. Cancer statistics, 2016. *Wiley Online Library*

118. Jun, Y., Huh, Y. M., Choi, J., Lee, J. H. & Song, H. T. Nanoscale size effect of magnetic nanocrystals and their utilization for cancer diagnosis via magnetic resonance imaging. *ACS Publications*

119. Yu, C., Fan, S. & Sun, Y. The potential of terahertz imaging for cancer diagnosis: A review of investigations to date. *ncbi.nlm.nih.gov*

120. Ono, H. Early gastric cancer: diagnosis, pathology, treatment techniques and treatment outcomes. *journals.lww.com*

121. Trautmann, A. Extracellular ATP in the immune system: more than just a “danger signal”. *Sci. Signal.* **2,** pe6 (2009).

122. Corriden, R. & Insel, P. A. Basal release of ATP: an autocrine-paracrine mechanism for cell regulation. *Sci. Signal.* **3,** re1 (2010).

123. Loo, J. M. *et al.* Extracellular metabolic energetics can promote cancer progression. *Cell* **160,** 393–406 (2015).

124. Di Virgilio, F., Ferrari, D. & Adinolfi, E. P2X(7): a growth-promoting receptor-implications for cancer. *Purinergic Signal* **5,** 251–256 (2009).

125. Pellegatti, P. *et al.* Increased level of extracellular ATP at tumor sites: in vivo imaging with plasma membrane luciferase. *PLoS One* **3,** e2599 (2008).

126. Pellegatti, P., Falzoni, S., Pinton, P., Rizzuto, R. & Di Virgilio, F. A novel recombinant plasma membrane-targeted luciferase reveals a new pathway for ATP secretion. *Mol. Biol. Cell* **16,** 3659–3665 (2005).